BMC Chemistry

RESEARCH Open Access

Combined experimental and theoretical investigation of the (benzoimidazol-2-yl)-methanone ligand and its Ru(III) complex: structural elucidation, stability determination, corrosion inhibition, energy storage and bioactivity applications

Hoda Abd El-Shafy Shilkamy[1*], Mehran Feizi-Dehnayebi[2], Senem Akkoc[2,3*], Sana M. Alahmadi[4], Moayad M. Khashoqji[4], Abeer N. Al-Youbi[4], Eida S. Al-Farraj[5] and Ahmed M. Abu-Dief[1,4*]

Abstract

Bis-(6-nitro-1H-benzoimidazol-2-yl)-methanone (NBM) ligand and its NBM-Ru complex act as corrosion inhibitors were synthesized and characterized utilizing various analytical, spectroscopic and physicochemical tools. Correlation between experimental data afford that NBM ligand acts as tri-dentate NNO ligand to give octahedral geometry of NBM-Ru complex. DFT calculations were applied to confirm the structure and reactivity of the investigated compounds as corrosion inhibitors. The NBM ligand and its ruthenium-bound derivative served as eco-conscious corrosion inhibitors, strategically slowing copper degradation through sustainable chemistry principles. For the corrosion testing phase, concentrated sulfuric acid solution (1 M) served as the primary aggressive environment. Electrochemical impedance spectroscopy and Tafel polarization techniques were employed to examine the corrosion resistance characteristics and suppression efficiency of NBM and its ruthenium-containing derivative within the acidic electrolyte under investigation. Our investigation explored how copper corrosion unfolds within acidic environments, specifically examining how the presence or absence of additives alters this chemical degradation process. "The experimental results reveal a compelling inverse relationship: as additive concentration increases, corrosion inhibition strengthens while the corrosive current density (Icorr) measurably diminishes. It is noted that inhibition efficiency increased and reached 97% and 98.9% in occupying of 1×10^{-4} and 1×10^{-6} M of NBM and NBM-Ru additives, respectively. Charge discharge behavior of Cu is also studied in some detail in

*Correspondence:
Hoda Abd El-Shafy Shilkamy
hoda_corr2012@science.sohag.edu.eg
Senem Akkoc
senemakkoc@sdu.edu.tr
Ahmed M. Abu-Dief
ahmedabudief@science.sohag.edu.eg

Full list of author information is available at the end of the article

© The Author(s) 2026. **Open Access** This article is licensed under a Creative Commons Attribution-NonCommercial-NoDerivatives 4.0 International License, which permits any non-commercial use, sharing, distribution and reproduction in any medium or format, as long as you give appropriate credit to the original author(s) and the source, provide a link to the Creative Commons licence, and indicate if you modified the licensed material. You do not have permission under this licence to share adapted material derived from this article or parts of it. The images or other third party material in this article are included in the article's Creative Commons licence, unless indicated otherwise in a credit line to the material. If material is not included in the article's Creative Commons licence and your intended use is not permitted by statutory regulation or exceeds the permitted use, you will need to obtain permission directly from the copyright holder. To view a copy of this licence, visit http://creativecommons.org/licenses/by-nc-nd/4.0/.

the absence and presence of additives. Moreover, the investigated compounds were screened for their biological activity against selected strains of bacteria and fungi and found to be more potent against *M. Luteus* bacteria and *C. albicans* fungi. Furthermore, Molecular docking was employed to evaluate the binding interactions of the free NBM ligand and its metal complex with the target biomolecule, providing insights into their potential biological activity and comparative affinity.

Keywords Imine complexes, DFT and molecular docking approaches, Electrochemical impedance spectroscopy, Biological evaluation

Introduction

Copper corrosion inhibition plays a critical role in the performance and longevity of modern electrochemical energy storage systems, particularly super capacitors and batteries. As one of the most widely used conductive materials in electrical applications due to its excellent conductivity and relatively low cost, copper faces significant challenges when exposed to the harsh electrochemical environments present in energy storage devices.

The electrochemical behavior of copper in super capacitors and batteries is fundamentally influenced by its susceptibility to oxidative corrosion processes [1, 2]. In these systems, copper components including current collectors, interconnects, and conductive additives are continuously exposed to electrolytes under varying potential conditions, leading to the formation of copper oxides and other corrosion products. These degradation processes can severely compromise device performance through several mechanisms: increased internal resistance due to the formation of poorly conductive oxide layers, mechanical degradation of electrode structures, contamination of electrolytes with dissolved copper ions, and ultimately, catastrophic failure of the energy storage system.

In super capacitors, where rapid charge-discharge cycles create dynamic electrochemical conditions, copper corrosion can lead to capacitance fade and reduced power density. The formation of copper oxide films on current collector surfaces increases the contact resistance between the active material and the current collector, directly impacting the device's ability to deliver high power outputs efficiently. Similarly, in battery systems, copper corrosion affects both the anode and cathode assemblies, where copper foils serve as current collectors. The dissolution of copper and subsequent re-deposition can create dendrites that may pierce separators, leading to internal short circuits and safety hazards [3–5].

Effective corrosion inhibition strategies for copper in these applications are therefore essential for maintaining optimal electrochemical performance, extending device lifespan, and ensuring operational safety. These strategies encompass various approaches, including the development of protective coatings, electrolyte additives, and advanced copper alloys with enhanced corrosion resistance. Understanding and controlling the electrochemical behavior of copper through proper corrosion inhibition techniques represents a crucial frontier in advancing the reliability and efficiency of next-generation energy storage technologies [6–10].

Schiff bases, characterized by the presence of the azomethine group (–C=N–), have attracted considerable attention as corrosion inhibitors because of their structural versatility, ease of synthesis, and strong ability to coordinate with transition metals [11]. Their inhibition efficiency is usually attributed to the electron density of the imine group, which facilitates adsorption on the metal surface, thereby forming a protective barrier that minimizes metal dissolution [12, 13]. Moreover, the introduction of substituents such as heteroatoms (N, O, S) or aromatic rings can further enhance their adsorption properties and interaction with metallic surfaces [14]. Recent advances in corrosion inhibition research highlight the important role of density functional theory (DFT) in understanding the adsorption behavior and inhibition mechanisms of organic compounds on metal surfaces. It has been established that key quantum chemical parameters, including HOMO–LUMO energies, energy gap (ΔE), and charge distribution, govern the interaction strength between inhibitor molecules and metal substrates. In particular, heterocyclic and Schiff base compounds exhibit excellent inhibition performance due to the presence of donor atoms and π-electron systems that facilitate strong adsorption. Recent studies further confirm the correlation between molecular electronic properties and inhibition efficiency, providing a theoretical foundation for structure–activity relationships [15, 16]. Complexation of Schiff base moieties with transition metals is a well-established strategy for improving their stability, solubility, and electronic properties, leading to enhanced corrosion inhibition performance. In particular, ruthenium (III) complexes have emerged as promising candidates because of the unique redox flexibility, coordination behavior, and catalytic attributes of Ru(III) [17]. These complexes often exhibit improved surface affinity, higher resistance to oxidative environments, and the ability to form more stable passive layers on metallic substrates compared with free ligands. The synergistic effect between Schiff base ligands and Ru(III) ions thus offers a promising platform for the design of efficient, durable, and environmentally friendly corrosion inhibitors. Investigating their adsorption

mechanism, inhibition efficiency, and surface interaction is crucial for developing advanced protective strategies for metals in aggressive environments. On the other hand, this coordination increases the lipophilicity of the compounds, facilitating their interaction with microbial cell membranes and improving their ability to penetrate and disrupt vital biological processes [18]. As a result, many Schiff base metal complexes exhibit superior antibacterial and antifungal activities compared to the free ligands, showing potential as effective alternatives to conventional antimicrobial drugs. Furthermore, the synergistic effect between the organic Schiff base and the central metal ion improves both the coverage and stability of the protective film, leading to excellent corrosion resistance in acidic and neutral environments. Thus, Schiff base ligands and their metal complexes serve as multifunctional materials bridging the gap between biological and industrial protection strategies [19].

The design of multifunctional coordination compounds has attracted considerable attention due to their ability to exhibit diverse properties arising from a common structural and electronic framework. In this context, the (benzoimidazol-2-yl)-methadone ligand and its Ru(III) complex represent a promising system in which heteroatom-rich coordination sites (N and O), extended π-conjugation, and a redox-active metal center collectively govern their physicochemical behavior. These features are known to strongly influence electron donation and back-donation processes, intermolecular interactions, and charge-transfer capabilities. Therefore, investigating corrosion inhibition, electrochemical energy storage, and biological activity within a single study is scientifically justified, as these applications are intrinsically linked through the same structure–property relationships. Such an integrated approach not only provides deeper insight into the fundamental behavior of the system but also supports the rational development of multifunctional materials with potential applicability across different technological and biomedical fields.

From this point of view, our work aimed to synthesize and Bis-(6-nitro-1 H-benzoimidazol-2-yl)-methanone ligand and its Ru(III) complex and characterize them by different physicochemical and analytical tools. Moreover, DFT and molecular docking approaches are applied to confirm their structure and biological efficiency. Furthermore, the efficiency of the inspected compounds as antimicrobial agents and corrosion inhibitors are investigated.

Experimental

Reagent

For the preparation of Bis-(6-nitro-1 H-benzoimidazol-2-yl)-methanone ligand, we exclusively employed high-purity reagents, including 4-nitro-o-phenylenediamine and diethyl 2-bromomalonate, which were used directly from the supplier without further purification. Our experimental protocol also included solvents such as ethanol, acetone, N,N'-dimethylformamide (DMF), and N, N'-dimethyl sulfoxide (DMSO), all of which were utilized in their original, unaltered state, thus obviating the need for distillation or additional purification measures. Materials and procedure of corrosion methods are represented in detail in supplementary data [20]. We explored copper's energy storage behavior in sulfuric acid baths (1 M concentration) under varying conditions. Using galvanostatic cycling a technique that controls electric current like a precision conductor we charged and discharged electrodes at six distinct intensity levels (± 1, ± 3, ±5, ± 10, ±20, ± 30 mA/cm^2). The study contrasted naked acid environments against those shielded by carefully measured doses of protective inhibitors, revealing how these chemical guardians alter charge-discharge processes.

Instrumentation

The study utilized an extensive collection of methodological resources and strategies, meticulously crafted to bolster the precision and trustworthiness of its conclusions. These supplementary materials constituted a robust framework that significantly contributed to the validity and credibility of the research outcomes.

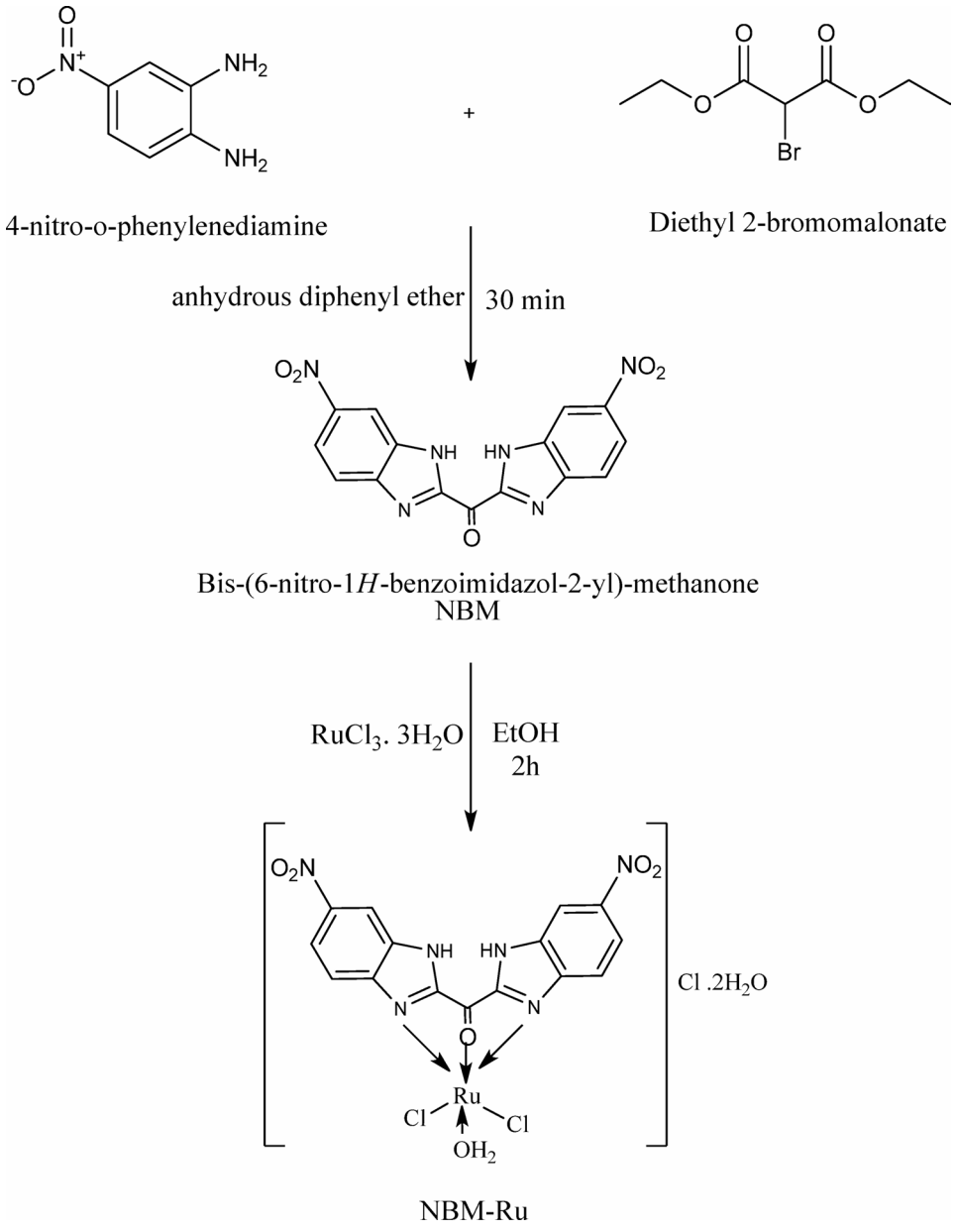
Synthesize of Bis-(6-nitro-1 H-benzoimidazol-2-yl)-methanone (NBM) ligand

A mixture of 4-nitro-o-phenylenediamine (0.765 g, 5 mmol) and diethyl 2-bromomalonate (1.20 g, 5 mmol) in anhydrous diphenyl ether (2 mL) was refluxed for 30 min., the solid product was precipitated on hot, collected by filtration, washed with petroleum ether (60–80) several times to remove unreacted materials recrystallized from ethanol to give dark-yellow powder (Scheme 1).

NBM ^{1}H-NMR (400 MHz, DMSO-d_6): d(ppm) 10.50 (s, 2 H, NH), 7.05–6.60 (m, 6 H, Arm). ^{13}C-NMR (δ, ppm) in DMSO-d_6: δ 163.68 (C = O), 132.15 (C = N), 124.59, 123.15, 117.76, 114.91, 113.38 and 72.24.

Synthesis of NBM-Ru complex

Bis-(6-nitro-1*H*-benzoimidazol-2-yl)-methanone chelate of $RuCl_3$. $3H_2O$ was prepared by refluxing equimolar ratios (1,1) in between the investigated Ru^{3+} cation (5 mmol, 1.3 g) and NBM ligand (5 mmol 1.76 g), were dissolved separately in EtOH (20 mL) and both solutions were combined in a hot environment. The mixed reactants were refluxed for 2 h after that kept for cooling at R.T. The precipitated products were separated out by filtration, washed with water, cold EtOH and Et_2O and finally dried under vacuum over $CaCl_2$ (Scheme 1).



Scheme 1 Diagrammatic approach to the NBM ligand and associated NBM-Ru complex

Determining the stoichiometry of ligand chelates via job's and molar ratio methods

This investigation employed ligand exchange and the modified Job's method in a solvent-based system to assess the stability and stoichiometry of metal-ligand interactions [21]. The absorbance spectra of the solutions were recorded progressively as the concentrations of the metal ion and the NBM ligand were varied. The mixture was subjected to a 10-minute sonication period after each addition to ensure thorough mixing and homogeneity of the components. The resulting data on absorbance was then plotted with respect to the ligand's mole fraction in the mixture, which is defined as the ratio of the ligand's molar concentration to the sum of the molar concentrations of the ligand and metal ion ([NBM] / [NBM] + [M]). Additionally, the data was analyzed in terms of the ligand-to-metal molar ratio ([NBM] / [M]). This approach facilitated an understanding of the interaction mechanisms and allowed for the determination of the most favorable stoichiometry for the formation of metal-ligand complexes.

Assessment of the apparent constant of complexes

Utilizing spectrophotometric techniques, the equilibrium formation constants of certain complexes were quantitatively established in meticulously prepared solutions.

This process strictly followed the guidelines and methodologies elucidated by Job, ensuring the accuracy and reliability of the obtained data [21]:

$$K_f = \frac{\frac{A}{A_m}}{C(1-A/A_m)^2} \quad (1)$$

Where there is 1:1 molar ratio.

Where Kf = formation constant of the metal–ligand complex ($L{\cdot}mol^{-1}$),

A = measured absorbance of the complex at a given concentration.

Am = maximum absorbance of the complex at saturation, The maximum absorbance Am was obtained from the Job's plot of absorbance versus mole fraction of the ligand (χ_ligand), ensuring the accurate determination of the 1:1 stoichiometry of the metal–ligand complex. This procedure allows reliable calculation of K_f using the spectrophotometric data.

initial molar concentration of metal ion.

To assess the change in free energy (ΔG) of the complexation reaction, the following relationship is typically used:

$$DG = -RT\ Ln\ K_f \quad (2)$$

Magnetic moment measurements

The evaluation of magnetic susceptibility represents an advanced analytical tool in the study of coordination complexes with transition metals, providing insight into their structural configurations [22]. This analytical method involves measuring the molar susceptibility of the complex, which necessitates the application of diamagnetic corrections to consider the presence of additional non-magnetic ions or molecules within the sample. The primary aim is to isolate and quantify the magnetic contribution of a single paramagnetic metal atom within the material being examined [23]. There are various strategies to compute these diamagnetic adjustments, with one commonly adopted approach grounded in Pascal's principles [22, 23].

$$\mu_{eff} = 2.83\sqrt{X_A.T} \quad (3)$$

$$X_A = X_M - (diamagnetic\ correction) \quad (4)$$

$$X_M = X_g\ .\ M.wt \quad (5)$$

The formula under consideration incorporates multiple variables, with T serving as the absolute temperature in Kelvin units, μ_{eff} representing the effective magnetic moment in Bohr Magnetons (denoted as B.M), X_g signifying the observed or experimental g-factor magnetic susceptibility, X_M indicating the initial molar magnetic permeability without adjustments, and X_A symbolizing the molar magnetic permeability after the necessary corrections have been applied.

Spectrophotometric studies

The UV-Vis spectroscopic analysis will be carried out across a comprehensive spectrum of wavelengths spanning from 200 nanometers to 800 nanometers. This specific range has been selected as it effectively captures the characteristic absorption bands commonly exhibited by metal complexes, which are frequently situated in the visible and ultraviolet regions of the electromagnetic spectrum. These absorption peaks are of particular significance as they are linked to the electronic transitions occurring within the metal centers of the complexes. By studying these spectral features, researchers can deduce valuable information regarding the metal-ligand bonding interactions, the structural configuration of the complex and the existence of any ligand-to-metal charge transfer (LMCT) or metal-to-ligand charge transfer (MLCT) phenomena.

Thermo-gravimetric analysis and kinetic studies

The thermal stability of a complex compound can be evaluated by conducting thermogravimetric analysis (TGA), which provides insights into the solvent's involvement in the coordination sphere and the overall structural integrity when subjected to varying temperatures. This technique is particularly useful in elucidating the role of solvent molecules within the complex and determining the material's stability under thermal conditions. To accurately assess the metal content within the mixture, it is essential to consider the kinetic aspects of the thermal degradation process, as these can significantly influence the observed weight loss patterns and rates. The Coats-Redfern method is a commonly employed approach for analyzing the kinetics of thermal degradation. This method, as outlined in the scientific literature by [24, 25], allows for the determination of the kinetic parameters such as activation energy (Ea) and frequency factor (A) from the TGA data. By applying the Coats-Redfern integral to the first-order reaction model, one can obtain the relationship between the fraction of the converted material (α) and time (t) as follows

$$\ln = \left[\frac{g(\alpha)}{T^2}\right] = \ln\left(\frac{AR}{\beta E}\right) - \frac{E}{RT} \quad (6)$$

where α is the fraction of the reacted material at time t, Ea is the activation energy, R is the universal gas constant, and T is the absolute temperature.

DFT and docking studies

DFT perspective

Computational studies based on density functional theory (DFT) were conducted with the Gaussian 09 W package [26], and the outcomes were visualized using GaussView 6.0. Geometry optimizations were achieved employing the B3LYP hybrid functional. For non-metal atoms (C, O, H, Cl, and N), the 6–311 g (d, p) basis set was applied, whereas the Ru^{3+} center was treated with the LANL2DZ basis set. To explore the electronic features of the NBM ligand and its Ru(III) complex, molecular electrostatic potential (MEP) mapping, frontier molecular orbital (HOMO-LUMO) analysis, and quantum chemical descriptors were determined. Furthermore, the compounds' reactivity and their anticorrosive potential were assessed through frontier orbital energy profiles and density of states (DOS) analysis.

Docking perspective

Molecular docking studies of NBM and Ru(III) complex with a bacterial and fungal receptors were carried out to complement the experimental assays. Docking calculations were performed using AutoDock 4.2 [27] along with AutoDock Tools 1.5.6 [28], which provided insights into binding poses and binding free energies (ΔG). The crystal structure of the sterol 14-alpha demethylase enzyme from Candida albicans (PDB ID: 5TZ1) and Micrococcus luteus (PDB ID: 1F75) was retrieved from the Protein Data Bank (www.rcsb.org/pdb) and prepared by eliminating water molecules, ligands, and non-essential atoms. All hydrogens were added, and Kollman charges were assigned to the receptor structure prior to docking. The geometries of the compounds were optimized computationally and employed as ligands in the docking process. A grid box ($104 \times 106 \times 104$ for 1F75 and $110 \times 98 \times 110$ for 5TZ1) with a spacing of 0.375 Å was centered on the active site of the targets to define the docking region. Simulations were executed using the Lamarckian Genetic Algorithm (LGA) with default parameters. The resulting docking conformations were analyzed, and the binding interactions were visualized with Discovery Studio Visualizer 4.1.

Biological evaluate

Antibacterial activity

The investigation assessed the antimicrobial efficacy of ligands and its metal complex in vitro against various microbial strains such as *Escherichia coli* and *Serratia marcescens* (Gram-negative bacteria), *Micrococcus luteus* (Gram-positive bacterium), as well as *Fusarium oxysporum*, *Candida albicans*, and *Aspergillus flavus* (fungi). The bacterial species were cultivated on nutrient agar and maintained under standard conditions at 37 °C for 24 h. Conversely, the fungi were propagated on malt extract agar and incubated at an optimal temperature of 28 °C for 48 h. The research employed the agar diffusion assay, a conventional method for evaluating the antimicrobial properties of substances [29, 30]. Prior to the experiment, equimolar stock solutions of the ligands and their metal complexes at a concentration of 1.0×10^{-3} M were prepared and sequentially diluted to 1.0×10^{-6} M with deionized water in a DMSO: H_2O ratio of 1:9. This dilution process ensured that the solutions were within a suitable range for testing. The microbial suspensions, adjusted to 0.80 g dm^{-3} NaCl, were mixed with the cooled, solidified culture medium at a ratio of 0.5 mL to 10 mL. The resulting mixture was uniformly spread over the surface of petri dishes to form a consistent layer. Next, 100 µL of the diluted ligand and complex solutions were dispensed into wells of 10 mm diameter that had been previously perforated in the inoculated agar. To establish a baseline for the experiment and to discern the antimicrobial activity of the ligands and complexes from any solvent-related effects or metal ion contributions, control tests, known as blank experiments, were performed. These controls were essential for distinguishing the specific antimicrobial properties of the compounds from any non-specific effects. Before the initiation of substantial microbial proliferation, the inoculated plates underwent a pre-incubation period of 4 h at 15 °C. This phase allowed for an even distribution of the antimicrobial substances throughout the agar medium. After pre-incubation, the plates were transferred to the appropriate temperature conditions conducive to the growth of the respective microbes. The zones of inhibition, which indicate the effectiveness of the ligands and complexes in halting microbial growth, were measured post-incubation.

$$\text{Antimicrobial activity index (A)} = \frac{\text{Inhibition area of compound (mm)}}{\text{Inhibition area for standard drug (mm)}} \times 100 \quad (7)$$

Result and discussion

Characterization of Bis-(6-nitro-1 H-benzoimidazol-2-yl)-methanone (NBM) ligand and its complex

In the absence of single-crystal X-ray diffraction data, the proposed octahedral geometry of the Ru(III) complex is supported by consistent spectroscopic and analytical tolls (FT-IR, CHN, UV–Vis, magnetic moment measurements and stoichiometry determination in solution) together with DFT-optimized structural parameters, all of which are in good agreement with reported six-coordinate Ru(III) systems.

Physicochemical characterization of the ligand and synthesized complex (Table 1) indicates structural integrity across analytical parameters. The compound adheres

Table 1 The synthesized ligand, denoted as NBM, and its corresponding metal complexes, chemical formulas, M.P, CHN, and IR frequencies

Compounds	Empirical formula (Formula weight)[a]	Color	(M. *p.*) and Decomp. Temp. (°C)	Λ_m (Ω^{-1} cm^2 mol^{-1})	μ_{eff} (B.M.)	Analysis (%) Found (Calc.)			IR, Cm^{-1}				
						C	H	*N*	)υOH)/ H_2O	υ(NH)	υ(C = O)	υ(C = *N*)	υ (M-O)	υ(M-*N*)
NBM	$C_{15}H_8N_6O_6$ (489.35)	Dark-Yellow	235	--	--	51.05 (51.14)	2.37 (2.29)	23.78 (23.86)	-	3213	1720	1647	-	-
NBM-Ru	$C_{15}H_{14}N_6O_8Cl_3Ru$ (613.5)	reddish Brown	> 300	62.75	3.75	29.41 (29.35)	2.39 (2.30)	13.60 (13.69)	3398	3206	1701	1633	530	470

to a 1:1 metal-ligand stoichiometric ratio, imparting robust stability under ambient atmospheric conditions and in the solid phase. Solubility profiling demonstrates extensive miscibility in diverse media, encompassing polar aprotic solvents (e.g., DMSO, DMF), organic phases (methanol, ethyl acetate), aqueous matrices, acetone, and standard laboratory solvents.

FTIR spectrum

Infrared spectroscopy provides critical insights into metal complex structures through analysis of vibrational modes arising from metal-ligand coordination bonds. When examining transition metal complexes, characteristic shifts in ligand absorption frequencies often indicate coordination site involvement. For the NBM-Ru complex, spectroscopic analysis reveals significant alterations compared to the free ligand precursor. Based on the spectroscopic analysis, the NBM ligand displays a characteristic vibrational band at 3213 cm^{-1}, attributed to the stretching mode of its NH functional group. This absorption feature persists with minimal spectral shift across all synthesized complexes [31]. The imine (–C = N) stretching vibration, originally observed at 1647 cm^{-1} in the uncoordinated ligand, undergoes a shift to 1633 cm^{-1} upon ruthenium coordination [32] (Table 1, Figure S1). Similarly, the carbonyl (–C = O) stretching frequency decreases from 1720 cm^{-1} to 1701 cm^{-1}, suggesting coordination through the carbonyl oxygen atom [33]. New vibrational modes emerge in the metal complex spectrum at 470 cm^{-1} and 530 cm^{-1}, attributed respectively to ν(Ru-N) and ν(Ru-O) stretching vibrations. These findings confirm coordination through both nitrogen and oxygen donor atoms [34]. Additionally, broadband absorption spanning 3398–3412 cm^{-1} corresponds to coordinated water molecules, supported by deformation modes at 738 cm^{-1} (rocking), 718 cm^{-1} (wagging), and 623 cm^{-1} (twisting) which confirm hydration sphere participation [35].

^{1}H-NMR & ^{13}C-NMR spectral evaluations

The ^{1}H-NMR spectrum of the Bis-(6-nitro-1H-benzoimidazol-2-yl)-methanone (NBM) ligand dissolved in DMSO-d_6 is depicted in Figure S2, where the aromatic protons exhibit resonances between δ 7.05–6.60 ppm (m, 6 H, corresponding to the aromatic ring moiety). Additionally, there is one signal observed at δ 10.50 ppm due to the presence of the 2NH protons, which disappear in D_2O. The ^{13}C-NMR spectrum of NBM confirm the structure of = ligand as Figure S3 exhibits signals at δ 163.68 (C = O), 132.15 (C = N), 124.59, 123.15, 117.76, 114.91, 113.38 and 72.24.

Elemental analysis and molar conductance

The proposed structural configuration of the synthesized complex received corroboration from complementary theoretical modeling and experimental CHN microanalytical data, indicating agreement between predicted and observed elemental composition. The NBM-Ru complex exhibited significant thermal resilience, as evidenced by its elevated melting point and decomposition temperature. Solubility assessments revealed that the isolated chelates dissolved readily in dimethylformamide (DMF) and dimethyl sulfoxide (DMSO). As presented in Table 1, the molar conductivity measurement for NBM-Ru (62.57 Ω^{-1} cm^2 mol^{-1}) aligns with established literature thresholds for mono-electrolytic complexes [36].

Electronic absorption spectra (EAS)

Ultraviolet-visible spectroscopy provides essential structural insights into metal coordination compounds. Analysis of spectral band positions and intensities reveals details about metal ion characteristics and molecular geometry. Figure 1 displays the room-temperature absorption spectra for both the NBM ligand and its ruthenium complex, with corresponding data in Table 1S. The NBM ligand spectrum shows three principal features: a π→π* transition at 273 nm, n→π* transitions at 290 nm and 395 nm associated with aromatic systems, and an intra-ligand transition near 410 nm [37]. Coordination with metal ions induces substantial spectral alterations, indicating electronic reorganization within the molecular framework and metal orbitals that confirm complex formation [38]. The NBM-Ru spectrum exhibits four distinct bands: π→π* (249 nm), n→π* (293 nm), ligand-to-metal charge transfer (396 nm), and (437 nm) [39]. An additional transition at 498 nm corresponds to d→d excitations characteristic of octahedral coordination environments [40]. The absorption band observed

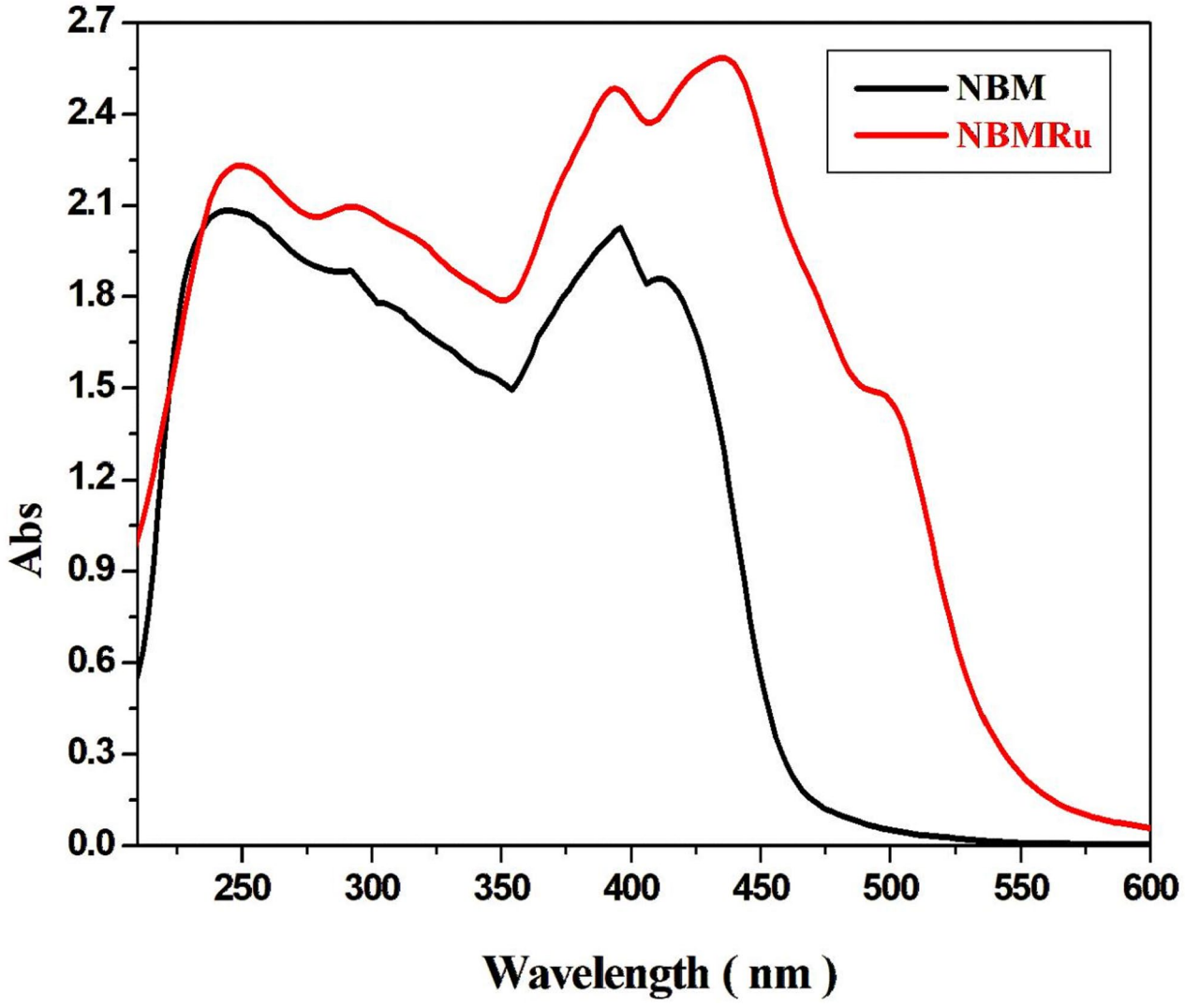


Fig. 1 Electronic absorption spectra of NBM ligand and its Ru complex in DMF at 298 K

at 498 nm in the NBT–Ru(III) complex is assigned to a spin-allowed d–d transition ($^2T_2g \rightarrow {}^2A_2g/{}^2T_1g$) in a low-spin octahedral Ru(III) (d^5) system, consistent with ligand field theory and Tanabe–Sugano considerations, and in agreement with reported spectral ranges for similar Ru(III) complexes [41].

Magnetic moment

The observed magnetic moment (3.75 B.M.) deviates from the expected spin-only value for a low-spin Ru(III) system (1.73 B.M.), which may be attributed to significant spin–orbit coupling effects and possible distortion from ideal octahedral geometry as confirmed by DFT calculation [42].

Thermal analysis

Thermal stability of the synthesized chelate compound was assessed via thermogravimetric analysis (TGA) under nitrogen atmosphere across a temperature gradient of 25–800 °C. Table 2 summarizes the observed mass loss percentages. For the NBM-Ru 1:1 complex, the TGA curve reveals four distinct decomposition phases: An initial mass decline of 11.60% (theoretical: 11.65%) from 30 °C to 175 °C, attributed to the release of two water molecules and one chloride [43]. A subsequent 14.54% reduction (theoretical: 14.50%) between 180 °C and 230 °C, corresponding to loss of one coordinated water molecule and two chloride ligands. Further decomposition between 235 °C and 380 °C resulted in a 28.99% mass decrease (theoretical: 29.01%), associated with elimination of the $C_7H_4N_3O_3$ moiety. Between 385 °C and 550 °C, 28.40% mass loss (theoretical: 28.36%) occurred due to removal of the $C_8H_4N_3O_2$ fragment. Beyond 560 °C, gradual decomposition stabilized at a residual mass of 16.43% (theoretical: 16.74%), consistent with ruthenium atom formation.

Kinetic aspect

Table 2 summarizes kinetic and thermodynamic parameters for metal chelate decomposition. Key observations emerge from the data: Negative entropy values (ΔS^*) reveal increased structural ordering in transition states relative to reactant species. The positive enthalpy values (ΔH^*) confirm endothermic reaction pathways. Elevated Gibbs free energy values (ΔG^*) across most decomposition stages indicate both non-spontaneous processes and reduced reaction kinetics, signifying higher energy states in residual products versus initial compounds. A notable compensation effect links activation energies (E^*) and pre-exponential factors (A) for these chelates. The modest A values imply inherently sluggish pyrolysis kinetics, while substantial E^* magnitudes suggest decomposition mechanisms involving significant transformations in vibrational, rotational, and translational energy states, alongside alterations in mechanical potential energy configurations [44].

Stoichiometry of complexes in solutions

The quantitative composition governing complex formation in solution specifically, the stoichiometric relationship between central metal ions and coordinating ligands determines fundamental coordination characteristics. Precise stoichiometric analysis of the NBM-Ru complex was conducted using two complementary approaches: Job's method of continuous variation and the mole ratio technique. Both methodologies yielded concordant results. In Job's method, systematic variation of metal-to-ligand mole fractions revealed characteristic absorbance deviations. Equimolar solutions of the metal ion and ligand were mixed in varying mole fractions while keeping the total concentration constant. The absorbance of each mixture was measured at the characteristic charge-transfer band of the complex. A plot of absorbance versus mole fraction of the ligand (χ_ligand) is shown in Figure X, which exhibits a clear maximum at χ_ligand ≈ 0.5. This indicates a 1:1 metal-to-ligand stoichiometry. All measurements were performed in triplicate, confirming the reproducibility and validity of the maximum absorbance point. This finding was corroborated by the mole ratio method, wherein absorbance plateau behavior confirmed identical stoichiometry. The convergence of results from independent analytical techniques validates the formation of the targeted mononuclear complex structure (Fig. 2) [17, 18, 45].

Table 2 Thermal decomposition steps, mass loss (%), proposed lost segments, and final residue thermo-kinetic activation parameters of each decomposition step for the prepared complexes

Complexes	Temp (°C)	Fragment loss %		Weight loss %		E^* ($KJmol^{-1}$)	A (S^{-1})	ΔH^* ($KJmol^{-1}$)	ΔG^* ($KJmol^{-1}$)	ΔS^* ($Jmol^{-1}K^{-1}$)
		Molecular formula	M. Wt.	Foundd	Calc					
NBM-Ru Residue	30–175	Cl $2H_2O$	71.5	11.60	11.65	24.50	0.01	23.65	51.91	-274.40
	180–230	2Cl coord+ H_2O	89	14.54	14.50			22.80	80.23	-280.13
	235–380	$C_7H_4N_3O_3$	178	28.99	29.01			21.94	109.27	-283.51
	385–550	$C_8H_4N_3O_2$	174	28.40	28.36			20.61	154.93	-286.99
	>550	Ru	101.07	16.43	16.47			-	-	-

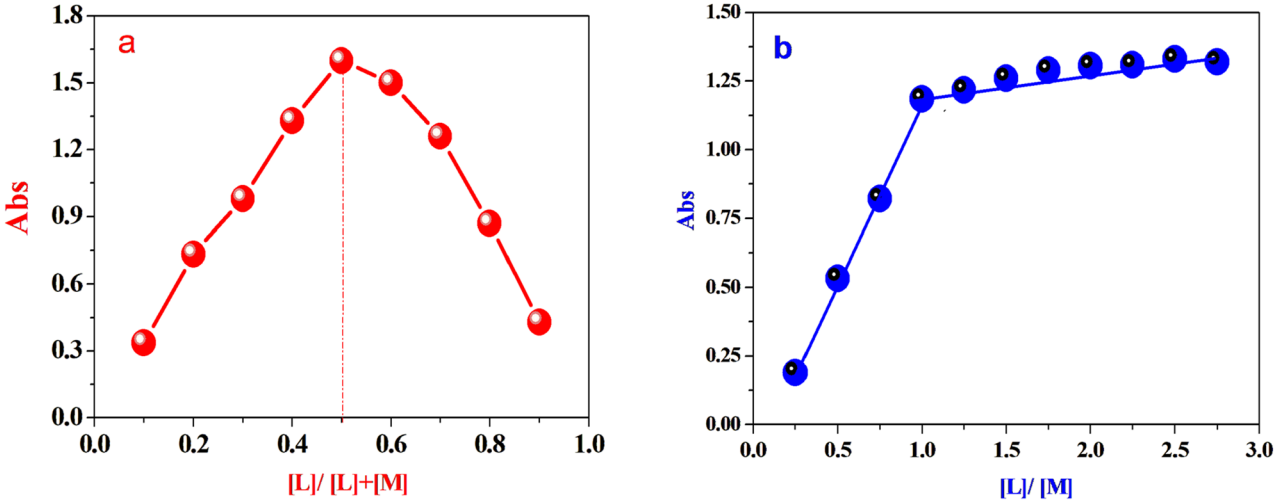


Fig. 2 Continuous variation and molar ratio plots for the prepared NBM-Ru complex in aqueous-ethanol at [NBM-Ru] = 1×10^{-3} M and 298 K

The apparent formation constants of the synthesized complexes

The formation constant (K_f) of the NBM-Ru complex was quantified via spectrophotometric analysis employing Job's method of continuous variation. The magnitude of K_f (7.75×10^4) indicates substantial thermodynamic stability for this complex. Complementary thermodynamic parameters, including Gibbs free energy changes (ΔG) and dissociation constants (pK), were additionally determined. The negative ΔG values (-27.89 $KJmol^{-1}$) confirm the spontaneous and energetically favorable nature of the complexation reaction [17, 18, 46].

pH profile of the investigated NBM-Ru complex

The NBM-Ru complex exhibits a pH-dependent stability profile, offering critical insights into its structural integrity across diverse pH environments. This characteristic holds significant relevance for catalytic applications, sensor design, and biological systems where pH fluctuations occur. As illustrated in Fig. 3, the complex demonstrates robust stability between pH 4–10, evidenced by minimal structural variation across this spectrum. Such consistency, coupled with an extended plateau region, supports deployment in environments with variable acidity/alkalinity without substantial decomposition. This resilience is particularly valuable for biochemical processes involving dynamic pH shifts. The sustained stability implies broad applicability in pharmaceutical formulation, agrochemical development, and ecological remediation strategies. Moreover, pH tolerance may enhance bioactive compound bioavailability, facilitating optimized delivery kinetics and target-site engagement in biological matrices [17, 18, 47].

DFT perspective

Optimized structures

The molecular geometries of NBM and its Ru(III) coordination complex (NBM-Ru) were optimized within the framework of DFT using the B3LYP functional in combination with a mixed basis set, 6–311 g (d, p) for non-metal atoms and LANL2DZ for the ruthenium center. These optimizations were carried out in the gas phase to gain insights into the intrinsic electronic structures of the free ligand and the metal-ligand assembly. The resulting equilibrium structures, depicted in Fig. 4, also include the atom-labeling scheme adopted for subsequent electronic analysis. DFT calculations confirm that upon chelation with Ru^{3+}, the metal center coordinates with two nitrogen atoms (N2 and N2′), one carbonyl oxygen (O3), two chloride atoms (Cl1 and Cl2), and one aqua ligand through the O4 atom. This coordination environment generates a distorted octahedral geometry around the ruthenium(III) ion, which is consistent with the preferred coordination mode of d^5 low-spin Ru(III) complexes. Key bond lengths and bond angles of the NBM ligand and its Ru(III) complex were examined to gain insight into their structural geometry and coordination behavior. For the free NBM ligand, the calculated bond lengths C1–N2, C1–N3, C1′–N2′, C1′–N3′, and C2–O3 are 1.310, 1.387, 1.310, 1.387, and 1.205 Å, respectively, while the bond angles N2–C1–N3 and N2′–C1′–N3′ are both 112.81°. Upon coordination with Ru(III), noticeable structural modifications occur. In the complex, the corresponding bond lengths C1–N2, C1–N3, C1′–N2′, C1′–N3′, and C2–O3 are 1.321, 1.388, 1.321, 1.388, and 1.207 Å, respectively, while the bond angles N2–C1–N3 and N2′–C1′–N3′ slightly increase to 112.84°. In particular, the elongation of the C1–N2 and C1′–N2′ bonds from 1.310 Å in the free ligand to 1.321 Å in the complex indicates electron density redistribution upon coordination to the Ru(III)

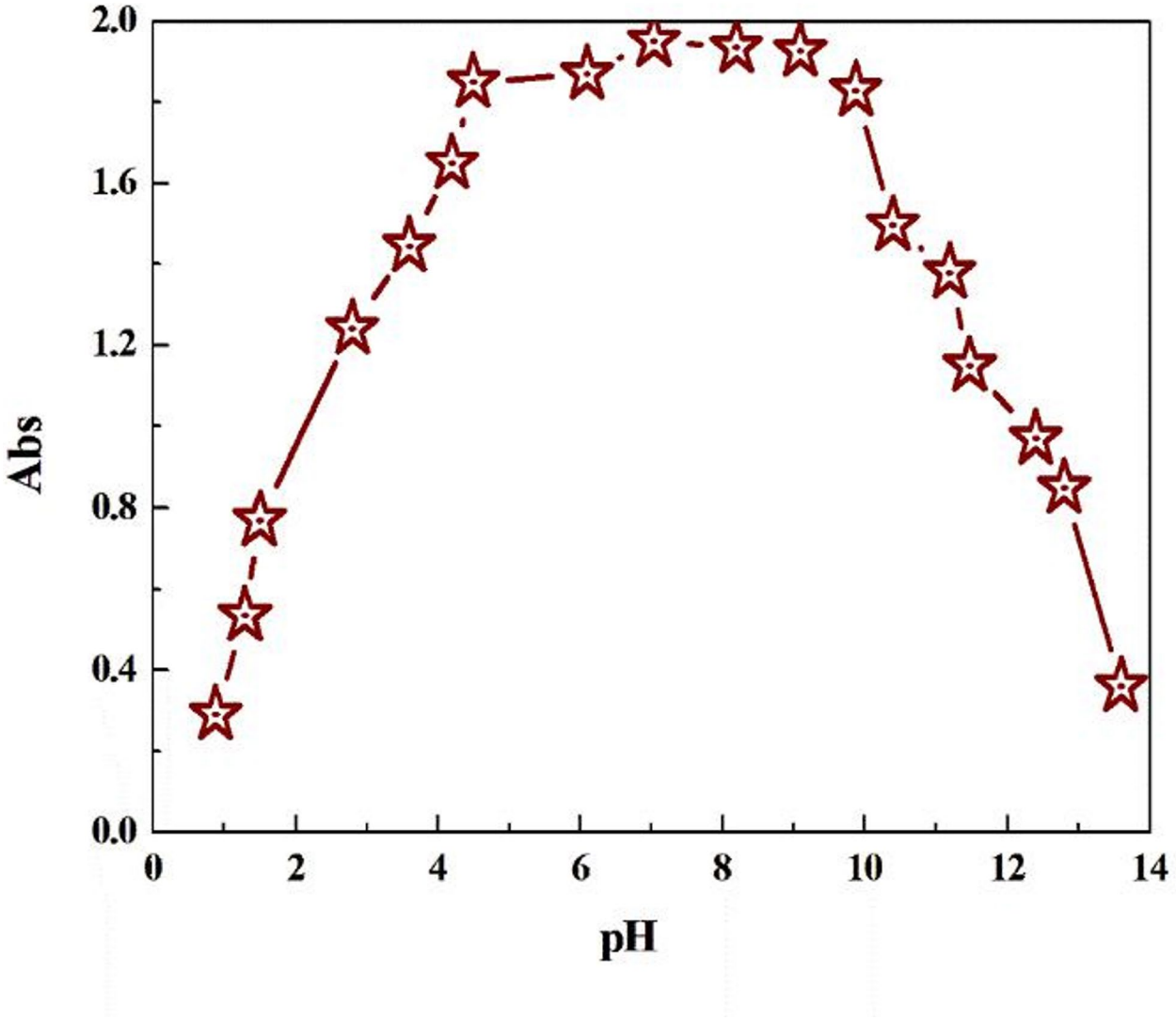


Fig. 3 The performances of pH on the complexing elements in an aqueous ethanolic media at 25 °C

center, leading to a slight weakening of these bonds. Such changes are characteristic of metal–ligand interactions and are consistent with previously reported coordination systems, thereby supporting the proposed coordination mode [48]. These results collectively confirm that the NBM ligand acts as a tridentate NNO donor, coordinating through two nitrogen atoms and one oxygen atom.

The optimized electronic energies of the isolated NBM ligand (-1281.18 Hartree) and the Ru(III) complex (-2372.40 Hartree) highlight the substantial stabilization gained upon coordination, demonstrating the thermodynamic favorability of complex formation. Furthermore, the calculated dipole moment of the Ru(III) complex (6.87 D) is markedly larger than that of the free NBM molecule (0.42 D). This considerable enhancement reflects the asymmetry introduced by metal-ligand bonding as well as the contribution of polar Ru–O and Ru–Cl bonds. The increased polarity is indicative of stronger intermolecular dipole-dipole forces [49], which not only improve solvation behavior but may also influence the electronic communication between the metal center and ligand framework. This electronic redistribution upon coordination is a key factor in modulating the structural stability, reactivity, and potential functional applications of ruthenium complexes in anticorrosion behaviors.

MEP guide

MEP mapping is a widely applied quantum chemical tool for pinpointing reactive domains within molecular frameworks [50]. This technique translates the spatial distribution of electrostatic potential into a color-coded surface, allowing straightforward visualization of electron-rich and electron-deficient regions. In such representations, red-shaded zones denote highly negative potentials, typically linked with regions prone to electrophilic attack, whereas blue regions signify electron-deficient domains

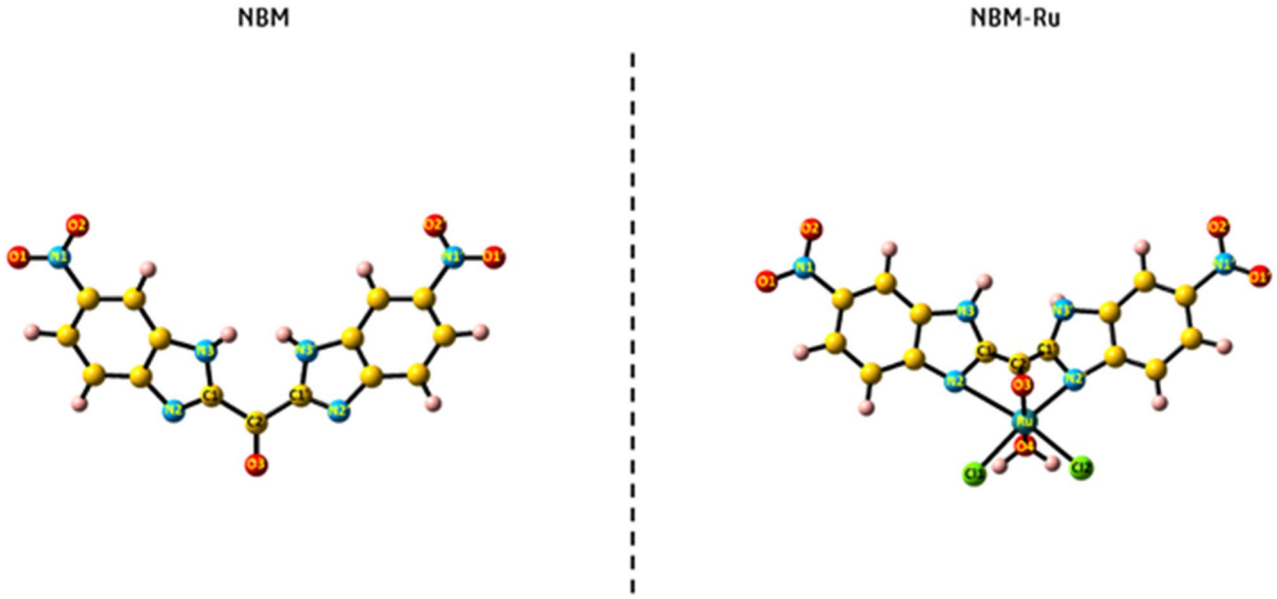


Fig. 4 Optimized structure of NBM and NBM-Ru

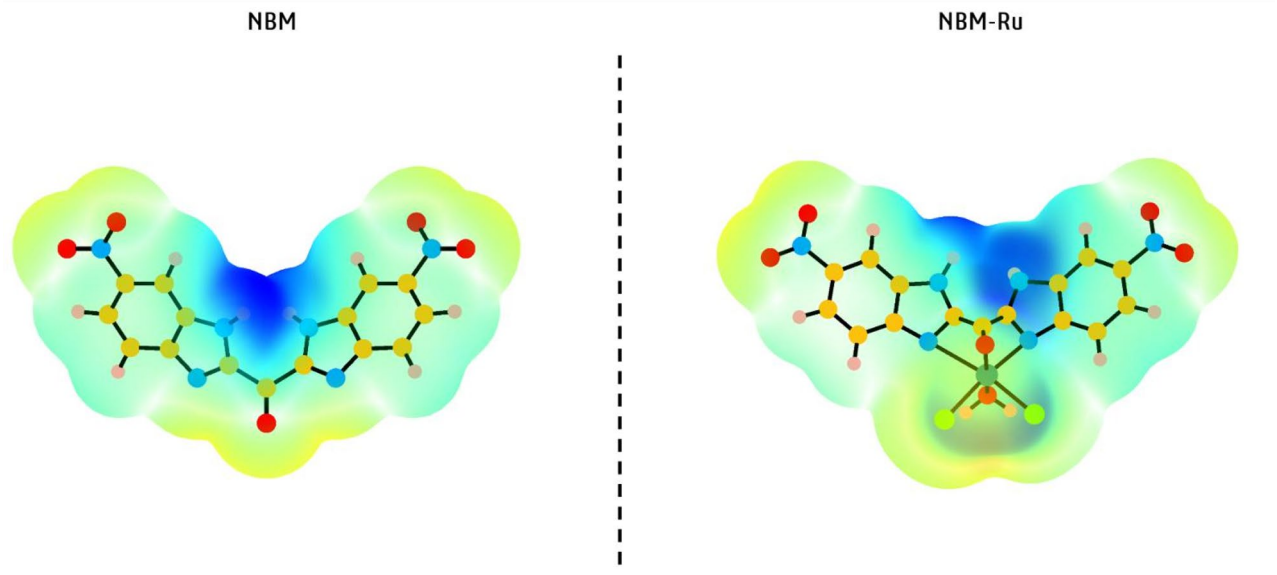


Fig. 5 MEP map of NBM and NBM-Ru using B3LYP level

that act as favorable sites for nucleophilic interactions [51]. Intermediate potentials are illustrated by gradations from orange to green, establishing the general trend: red < orange < yellow < green < blue [52]. The MEP surfaces of the NBM and NBM-Ru were obtained within the DFT framework, and the corresponding maps are displayed in Fig. 5. For the uncoordinated ligand NBM, a pronounced electron density localization is observed around the heteroatoms, particularly nitrogen and oxygen. A broad red-to-yellow contour extends over the vicinity of atoms N2, N2′, and O3, which is attributable to the presence of nonbonding electron pairs. This feature strongly supports their role as Lewis basic centers, thereby providing favorable binding sites for electrophilic species or coordination to transition-metal cations [53] such as Ru^{3+}. The visualization thus rationalizes the experimental observation of ruthenium binding in this region. Conversely, the surface of the NBM ligand also exhibits blue coloration near hydrogen atoms bonded to nitrogen atoms, indicating electropositive domains. These areas can engage in hydrogen bonding or function as potential docking points for nucleophilic reagents. Upon coordination with ruthenium, the electrostatic landscape of NBM-Ru undergoes a redistribution. In

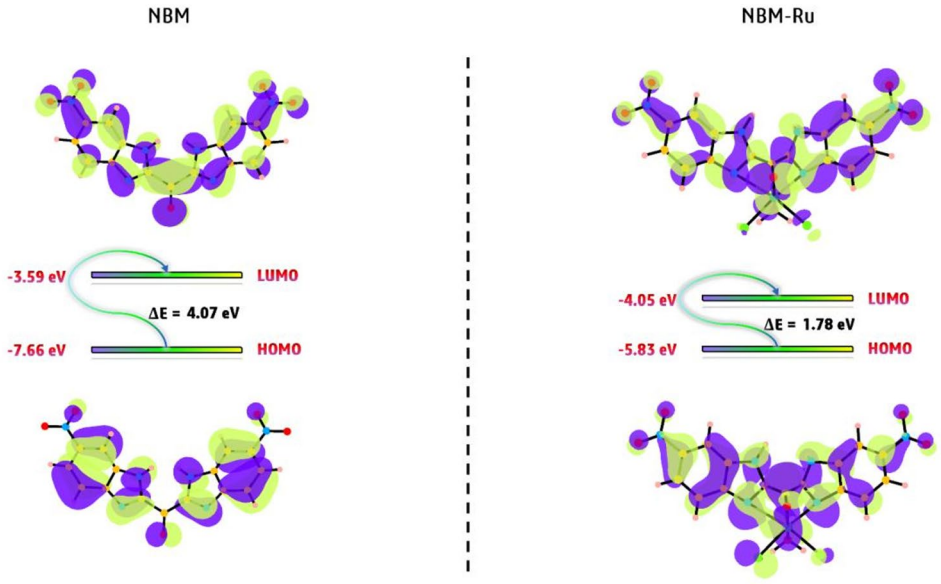


Fig. 6 Distribution of FMO for NBM and NBM-Ru using B3LYP level

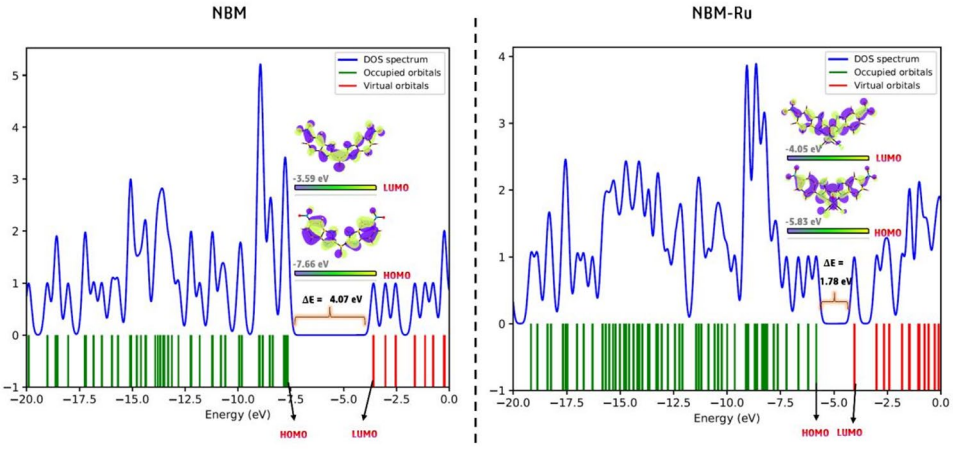


Fig. 7 DOS spectrum of NBM and NBM-Ru

this complex, the electropositive character becomes particularly evident on the hydrogens attached to the nitrogen atoms as well as on the oxygen atom of coordinated water. Such features imply that, within the metal-bound system, these protons and oxygen atoms constitute favorable loci for nucleophilic interactions. The observed shift in the potential profile upon metal complexation highlights how coordination alters electronic properties.

Molecular orbitals theory and DOS analysis

The concept of frontier molecular orbitals (FMOs) encompasses both the HOMO and LUMO. The HOMO describes the electron-donating capability of a molecule, while the LUMO characterizes its propensity to accept electrons, thus together governing the fundamental aspects of molecular reactivity and electronic transitions. Examination of the FMO characteristics of NBM and its Ru(III)-coordinated derivative (NBM-Ru) provides valuable insight into their electronic behavior and reactivity descriptors. It is well established that compounds with narrower HOMO-LUMO separations display higher softness, increased polarizability, and enhanced chemical reactivity, albeit at the expense of kinetic stability [17, 18]. As shown in Fig. 6, the calculated HOMO-LUMO gap for NBM and NBM-Ru are 4.07 and 1.78 eV, respectively, in the gas phase. The pronounced reduction in band gap upon complexation with Ru(III) suggests that the metal center plays a decisive role in lowering the excitation barrier, thereby enhancing the electronic response of the complex relative to the free ligand.

To further quantify the orbital contributions, density of states (DOS) spectra was generated using the GaussSum package at the B3LYP level of theory (Fig. 7). In the DOS plots, HOMO states are represented in green, while

LUMO levels are indicated in red. For pristine NBM, the HOMO and LUMO were localized at -7.66 and – 3.59 eV, with a band gap of 4.07 eV. In contrast, the NBM-Ru complex exhibited HOMO and LUMO levels at -5.83 and – 4.05 eV, respectively, narrowing the energy gap to 1.78 eV. This marked decrease is fully consistent with the trends predicted by FMO analysis and underscores the crucial role of Ru(III) in modulating the electronic structure of the ligand framework. From a corrosion inhibition perspective, a smaller HOMO-LUMO gap is highly advantageous. The enhanced electronic softness of the Ru(III) complex facilitates more effective charge transfer interactions with metallic surfaces, thereby strengthening adsorption and forming a protective layer that hinders oxidative degradation. Such electronic adaptability aligns with the general principle that molecules with low energy gaps are superior inhibitors, as they can readily engage in donor-acceptor interactions with the d-orbitals of metal substrates. Consequently, the significant reduction in band gap observed for the NBM-Ru system provides compelling evidence for the Ru(III) complex's superior anti-corrosion performance compared to the parent NBM ligand.

Quantum parameters and corrosion inhibition

A key approach to evaluating the performance of corrosion inhibitors is the investigation of their electronic descriptors, which directly influence molecular reactivity and interaction with metallic surfaces. For this purpose, quantum chemical calculations were conducted on NBM and its Ru(III) complex (NBM-Ru). Several global reactivity parameters, derived from the HOMO and LUMO energies, were determined, including electronegativity (χ), chemical hardness (η), softness (σ), chemical potential (Pi), electrophilicity index (ω), and the maximum charge transfer parameter (ΔNmax). These indices, calculated using well-established definitions [54], are summarized in Table 3. The comparison between NBM and NBM-Ru reveals a distinct enhancement in the electronic properties of the Ru(III) complex. The marked reduction in energy gap (ΔE = 1.78 eV for NBM-Ru vs. 4.07 eV for NBM) indicates that the Ru(III) complex is far more polarizable and chemically reactive. According to the hard-soft acid-base principle, softer molecules exhibit stronger interactions with metallic substrates, which are typically considered soft acids [55]. Thus, the higher softness (σ = 1.12 eV) and lower hardness (η = 0.89 eV-1) of NBM-Ru compared to NBM (σ = 0.49 eV, η = 2.03 eV-1) strongly suggest that the Ru(III) complex possesses superior adsorption capability on metal surfaces. Furthermore, the upward shift in HOMO energy from – 7.66 eV in NBM to -5.83 eV in NBM-Ru implies that the complex has a greater tendency to donate electrons to vacant orbitals of the metal. This is consistent with the larger ΔN_{max} value observed for NBM-Ru (5.55) relative to NBM (2.77), reflecting an enhanced electron transfer process from the inhibitor to the metal surface [56]. Since electron donation is a key mechanism for forming a protective barrier, this parameter confirms the stronger inhibitory nature of the Ru(III) complex. In addition, the global electrophilicity index (ω) nearly doubles upon coordination with Ru(III), rising from 7.78 eV for NBM to 13.71 eV for NBM-Ru. A high electrophilicity index suggests an increased capacity to stabilize charge transfer interactions during adsorption, thereby improving the ability of the inhibitor to protect the metal from oxidative attack. As a results, these quantum chemical descriptors establish that NBM-Ru is electronically better suited for corrosion inhibition than the parent ligand. Its reduced band gap, higher softness, enhanced electron-donating ability, and elevated electrophilicity all converge to promote strong, stable adsorption on the metal surface, thereby making the Ru(III) complex a highly promising anti-corrosion agent.

Table 3 Quantum reactivity parameters of NBM and NBM-Ru

descriptor	NBM	NBM-Ru
E_{HOMO}	-7.66	-5.83
E_{LUMO}	-3.59	-4.05
$\Delta E_{(LUMO-HOMO)}$	4.07	1.78
χ	5.62	4.94
η	2.03	0.89
σ	0.49	1.12
P_i	-5.62	-4.94
ω	7.78	13.71
ΔN_{max}	2.77	5.55

Potentiodynamic polarization curves

Potentiodynamic polarization curves map a material's electrochemical behavior like a fingerprint reveals identity—distinct, revealing, impossible to replicate. Imagine slowly nudging voltage across a metal surface immersed in electrolyte while measuring current response. This dance between applied potential and resulting current unveils corrosion rates, passivation thresholds, and pitting susceptibilities in a single sweep. The polarization behaviors of copper in 1 M H_2SO_4 in deficiency and occupying of various doses 1×10^{-6}, 5×10^{-6}, 1×10^{-5}, 5×10^{-5} and 1×10^{-4} M of NBM and NBM-Ru complex as inhibitors is shown in Fig. 8a, b. Key electrochemical parameters were determined, including corrosion potential (E_{corr}), anodic and cathodic Tafel slopes (βa, βc), corrosion current density (I_{corr}), and inhibitor efficiency. When we introduce the tested corrosion blockers, the metal's electrochemical decay rate drops significantly below levels seen in the untreated solution. Thus, the copper develops a self-shielding barrier that naturally coats its exterior. In the occupying of 1×10^{-6} M of NBM,

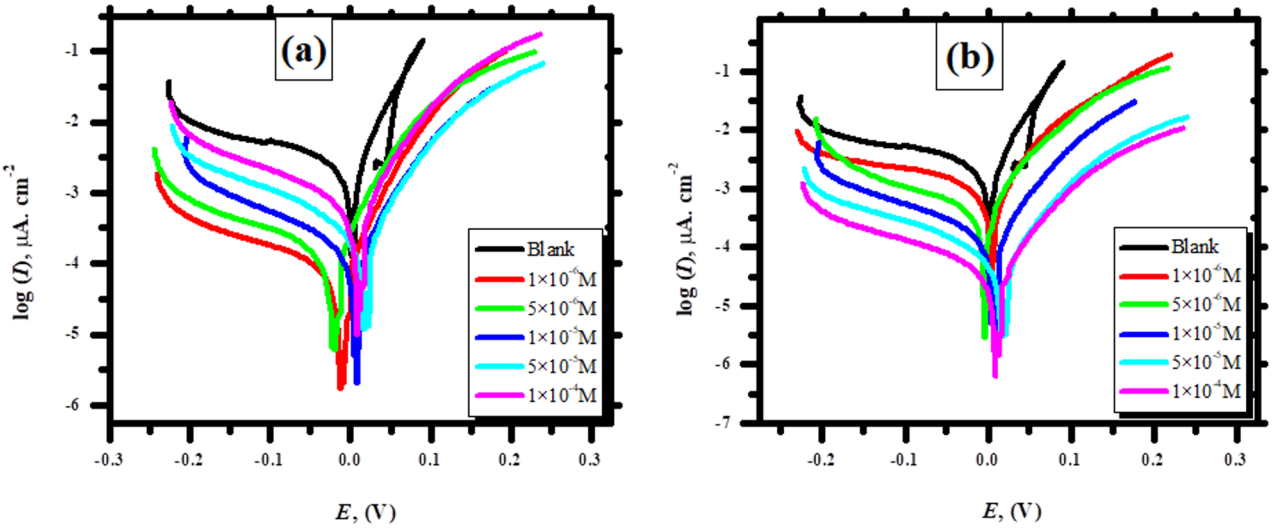


Fig. 8 At 25 °C, the Tafel plot curvatures for Cu in 1 M H_2SO_4 with distinct dosages of NBM (**a**) and NBM-Ru (**b**) are shown

Table 4 Cu metal's Tafel constants in 1 M H_2SO_4 in distinct proportions of the NBM and NBM-Ru complexes at 25 °C

$C_{inh.}$	E_{corr} (V)	I_{corr} (µA cm^{-2})	β_a (V/decade)	β_c (V/decade)	Θ	η %
	In the presence of NBM					
Blank	0.018	3467.4 ± 0.70	28.34	-2.55	-	-
1×10^{-6} M	0.006	100.7 ± 0.50	26.2	-4.10	0.97	97 ± 0.5
5×10^{-6} M	-0.007	134.9 ± 0.40	28.1	-4.14	0.96	96 ± 0.5
1×10^{-5} M	0.012	148.3 ± 0.30	30.0	-1.30	0.957	95.7 ± 0.3
5×10^{-5} M	0.029	190.5 ± 0.30	18.7	-4.2	0.945	94.5 ± 0.3
1×10^{-4} M	0.024	537.0 ± 0.45	16.6	-4.5	0.845	84.5 ± 0.4
	In the presence of NBM-Ru					
1×10^{-6} M	0.028	1288.2 ± 0.45	34.3	-2.1	0.628	62.8 ± 0.5
5×10^{-6} M	0.0098	390.8 ± 0.57	34.1	-2.40	0.887	88.7 ± 0.5
1×10^{-5} M	0.015	129.1 ± 0.67	28.6	-4.4	0.963	96.3 ± 0.4
5×10^{-5} M	0.029	48.6 ± 0.35	22.1	-3.4	0.986	98.6 ± 0.3
1×10^{-4} M	0.023	36.2 ± 0.20	21.7	-3.9	0.989	98.9 ± 0.3

the corroding current density has been lessened then rises again with standing up the inhibitor dose in the range of 5×10^{-6} to 1×10^{-4} M. It is argued that the high concentrations of NBM is insufficient to produce a protective film (covering the entire copper exterior side) and the optimum dosage of NBM is 1×10^{-6} M. As the NBM concentration stands up, both the anodic and cathodic current densities rise but still less than that of those in the 1 M H_2SO_4 solution. In the case of using NBM-Ru complex, the corroding current density lessens gradually with standing up the dose. This behavior indicates the exterior coverage has been enhanced in the presence of high dosages of complex. The corroding potential (E_{corr}) values generally shift to negative in the presence of some concentrations then shifted to the positive direction in the case of the two inhibitors. Additionally, the anodic (β_a) and cathodic (β_c) Tafel slopes are changed in occupying of NBM inhibitor, as shown in Table 4. This behavior can be explained on the basis that a protective layer formed on the metal exterior side [57]. Table 4 show the E_{corr} values changes with pushing up inhibitor dose. NBM acts as a mixed-type inhibitor, with a corrosion potential displacement of less than 85 mV [58]. The percentage of inhibitory effectiveness (IE%) are calculated using (Eq. 8) and registered in Table 4. Adsorption isotherms are utilized to understand corroding adsorption processes. Experimental data were fitted to number of adsorption isotherms, including Langmuir, Frumkin, Temkin, as well Freundlich, in order to elucidate kind and strength of adsorption. Plotting C_{inh}/θ vs. C_{inh} (Fig. 5S) produces linear graph with correlation coefficient greater than 0.99993 as well slope near unity, assuming that Langmuir adsorption isotherm is followed by NBM and NBM-Ru adsorption in the tested solution on Cu surface.

$$\eta/\% = \frac{(I_{\text{uninhi.}} - I_{\text{inhib.}})}{I_{\text{uninhib.}}} \times 100 \quad (8)$$

Electrochemical impedance spectroscopy

Electrochemical Impedance Spectroscopy (EIS) is a powerful analytical technique widely used to investigate interfacial properties and charge transfer processes in electrochemical systems. It also help to investigate the mechanism of corrode inhibition. Figure 9a, b manifests Nyquist graph for copper in 1 M H_2SO_4 solutions in the deficiency and occupying of various doses of NBM and its complex as corrode inhibitors at room temperature. The complex plane of impedance plot at E_{corr} is shown in Fig. 9. The impedance spectra recorded using copper as the anode consistently display a single capacitive loop, regardless of whether inhibitor concentrations are altered or absent. The distinct semicircular pattern observed in the spectral analysis indicates active corrosion occurring where the electrolyte contacts the outer surfaces. Figure 9a and b demonstrate significant alterations in copper's impedance response when varying concentrations of additives were introduced into the corrosive solution. This can be explained by the fact that the lowest dose of NBM inhibitor cause rise in substrate impedance. As well, the highest dosage of NBM–Ru causes moving up in charge transfer resistance more than the other inhibitor doses. The semicircles have ideal capacitive behavior. As the dosage of NBM additive increases to 1×10^{-4} M charge transfer resistance decreases but still higher than that of Cu in pure medium. In the occupying of high NBM-Ru inhibitor dose 1×10^{-4} M, the charge transfer resistance has high value than that obtained at all other NBM-Ru dosages. These outcomes are discussed on several fundamental mechanisms such as improved surface coverage - Higher inhibitor dosages lead to more complete coverage of the metal exterior, blocking a greater

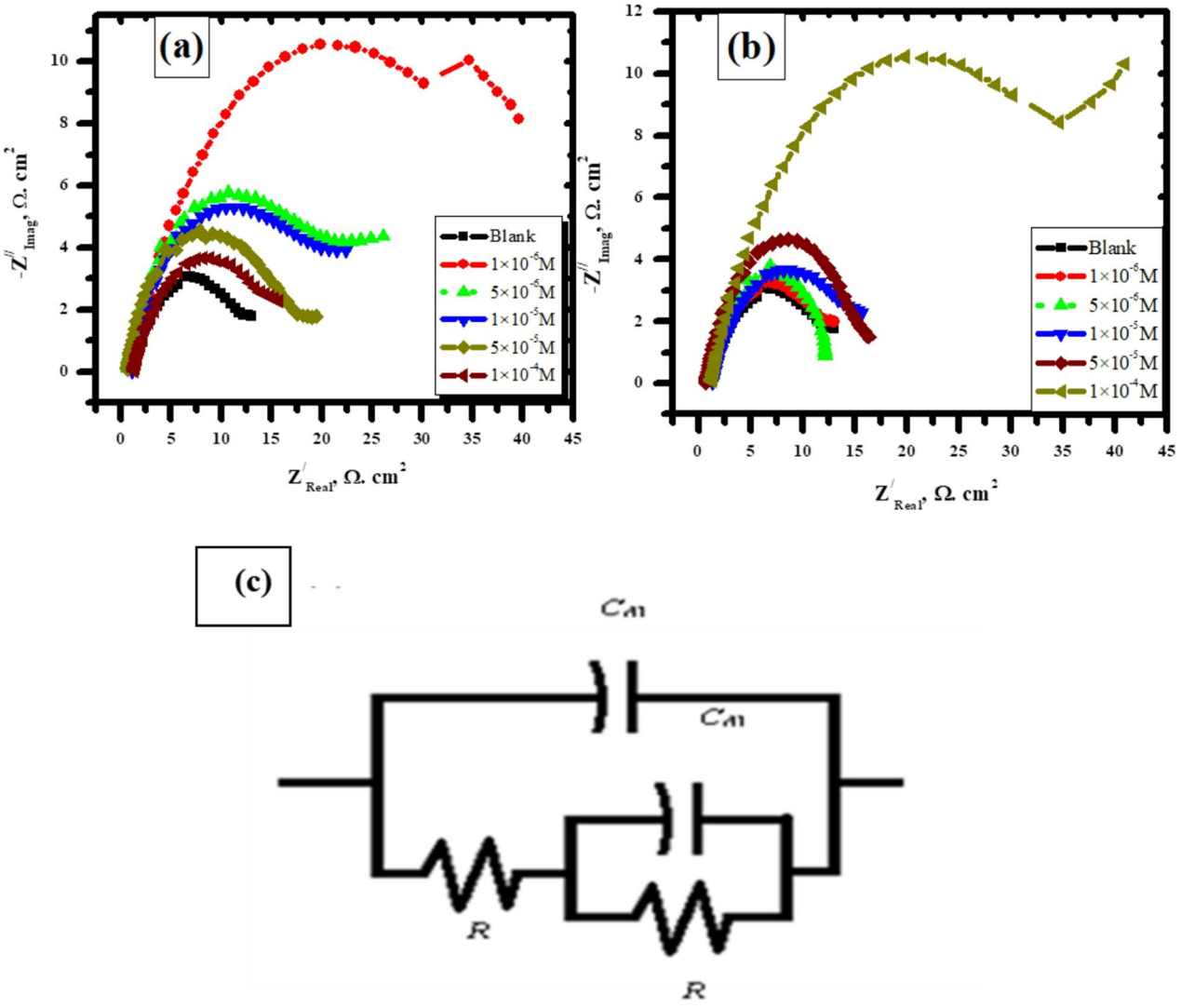


Fig. 9 Nyquist plots of Cu in 1 M H_2SO_4 at varying dosages of NBM (**a**) and NBM-Ru (**b**) at 25 °C Equivalent circuit fitting impedance data (c)

percentage of active corrode spots. This directly stands up the charge transfer resistance as fewer sites remain available for electrochemical reactions. Also, formation of more robust protective films - At higher dosages, inhibitors can form more dense, continuous, and defect-free protective films on metal exterior. These films create a more effective barrier against charge transfer processes. In addition, multi-layer adsorption - Higher dosages of NBM-Ru can enable the formation of multiple inhibitor layers, creating a thicker protective barrier that electrons must traverse, thereby standing up the resistance to charge transfer. So that, semicircle obtained in occupying of the high NBM-Ru dosage (1×10^{-4} M) is the best semicircle get at all dosages [59, 60]. The double layer capacitance C_{dl}. also steadily drops in the aforementioned sequence when NBM-Ru additive dosage is raised. In the case of using NBM additive the lowest value of C_{dl} was obtained in the occupying of 1×10^{-6} M. The estimated parameters of electrochemical impedance are listed in Table 5. Plots of Nyquist, bode plots, as well phase bode plots for Cu in 1 M H_2SO_4 at varying dosages NBM additive 1×10^{-6}, 5×10^{-6}, 1×10^{-5}, 5×10^{-5} and 1×10^{-4} M at 25 °C are displayed in Fig. 10.

In Bode plot representations, impedance magnitude (expressed logarithmically as log |Z|) and phase shift (θ) are graphed as functions of logarithmic frequency (Fig. 10a, b, c, d). The impedance curves for copper without inhibitor exhibit identical characteristics to those with inhibitor present. However, the addition of NBM-Ru inhibitor concentrations causes a distinct shift toward higher resistance values, as shown in Fig. 10b. This means that the corrode mechanism of copper alloy doesn't change in 1 M H_2SO_4 solution in lack and occupying of inhibitor [61]. Table 5 shows the EIS variables for Cu in 1M H_2SO_4 in the lack and occupying of NBM and NBM-Ru inhibitors. The Nyquist graph manifested that the impedance response of copper changes significantly in occupying of the NBM and NBM-Ru inhibitors in 1 M H_2SO_4 solution, as shown in Fig. 110a-d. In the occupying of NBM, the IE value has highest value at 1×10^{-6} M. The radius of Nyquist plots develops as the dosage of NBM-Ru inhibitor rises; nevertheless, this shift has minimal effect on the shape of Nyquist plots. Furthermore, the solution resistance (R_s) has nearly the same value at all the inhibitor concentrations. The observation suggests a shielding film develops on the copper surface, alongside the theory that copper degradation is governed by electron movement processes [62]. The impedance curves generated for Cu in 1 M H_2SO_4 in the lack and occupying of distinct dosages of NBM and NBM-Ru inhibitors form perfect semicircles, as shown in Fig. 9. The homogeneity on the electrode exterior sides outcomes in perfect semicircle [63].

Table 5 The electrochemical impedance parameters for copper metal in 1 M H_2SO_4 at 25 °C with multiple NBM and NBM-Ru dosages

In the presence of NBM			
$C_{inh.}$	$R_s\,\Omega$	$R_{ct}\,\Omega$	C_{dl} F
Blank	0.83	13.0	1.22×10^{-6}
1×10^{-6} M	0.20	52.0	3.06×10^{-7}
5×10^{-6} M	0.20	25.8	6.17×10^{-7}
1×10^{-5} M	0.20	25.0	6.36×10^{-7}
5×10^{-5} M	0.10	20.1	7.92×10^{-7}
1×10^{-4} M	0.31	17.3	9.19×10^{-7}
In the presence of NBM-Ru			
1×10^{-6} M	0.8	14.6	1.09×10^{-6}
5×10^{-6} M	0.8	15.2	1.05×10^{-6}
1×10^{-5} M	0.8	16.7	9.53×10^{-7}
5×10^{-5} M	0.8	20.1	7.92×10^{-7}
1×10^{-4} M	0.8	57.6	2.76×10^{-7}

Morphology of the surface

After soaking a copper sample for a full day in concentrated sulfuric acid, we studied its transformed outer landscape using electron microscopy paired with elemental mapping. Figure 11a shows copper exterior morphology after exposure to the H_2SO_4 solution in the lack of inhibitors, while (Fig. 11b, c) illustrates exterior morphology in the occupying of 1×10^{-6} and 1×10^{-4} M of NBM-Ru inhibitor, respectively. The SEM images are coupled with EDX analysis in Fig. 12a, b, c to distinguish elements present on copper exterior in the lack and occupying of the inhibitor. Surface attack and damage due to sulphate ions is recognized, indicating the occurrence of corrode, as shown in Fig. 11a. Figure 12a shows the EDX spectrum without the inhibitor. It shows oxygen, sulphur, and copper. This indicates that corrosion processes lead to the formation of copper oxides and sulphates.)Fig. 11b(demonstrates a notable reduction in surface degradation when the inhibitor concentration reaches 1×10^{-6} M. A protective film forms on the copper surface, visibly shielding the material. This protective effect intensifies significantly at the higher concentration of 1×10^{-4} M NBM-Ru, as evidenced in Fig. 11c, where the film appears more pronounced and uniformly established. The EDX data in Fig. 12b confirms carbon presence and significant oxygen depletion, with the dominant carbon peak originating from the inhibitor compound. The percentage of carbon has been raised and Ru element has been appeared in EDX chart in existence of high dosage of NBM-Ru (1×10^{-4} M) in Fig. 12c.

Charge discharge studies

Charge-discharge studies are fundamental for evaluating the electrochemical performance of materials, especially in applications like batteries, super capacitors, and energy storage systems. These studies provide insights into the

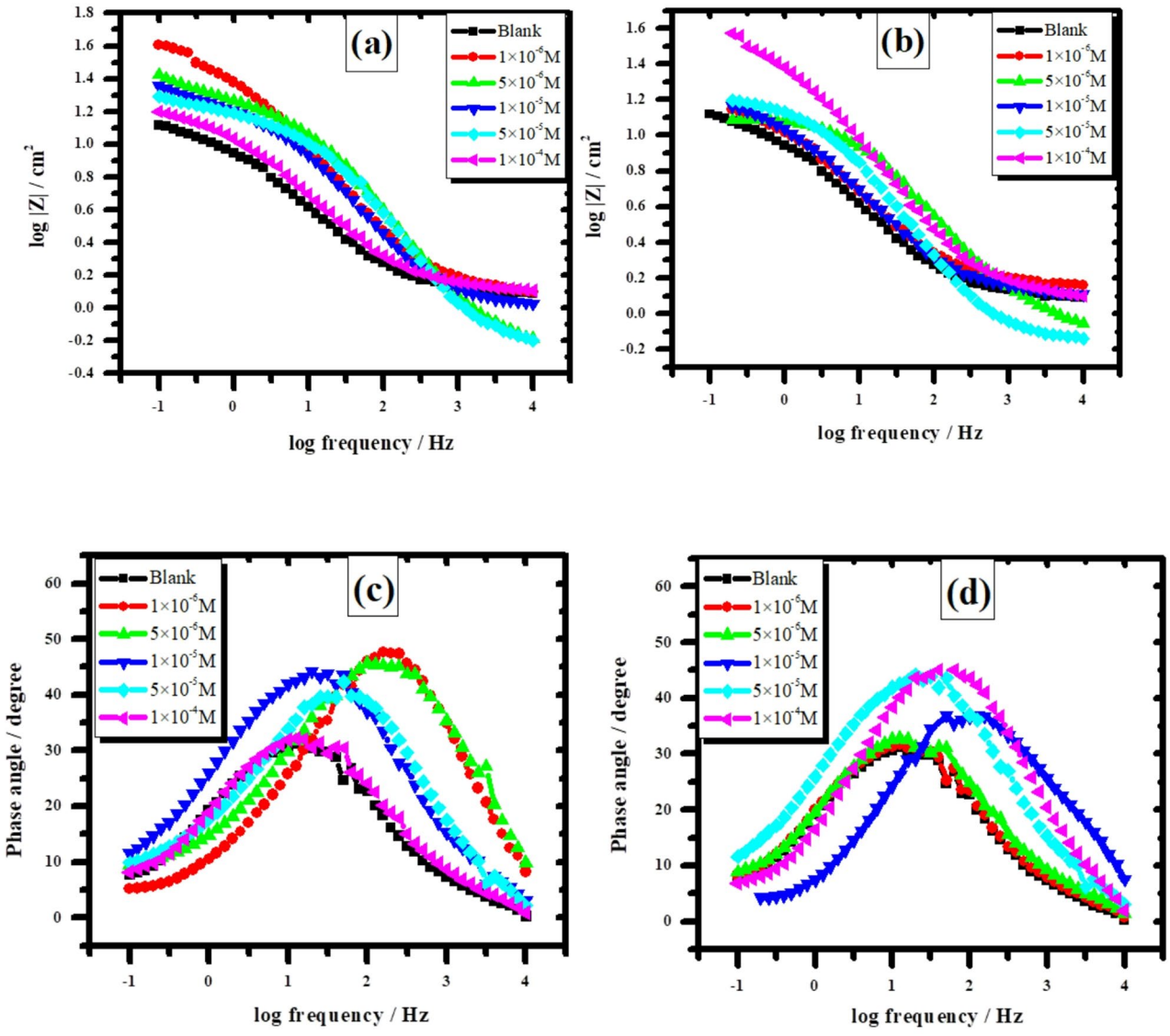


Fig. 10 Bode plots of Cu in 1 M H_2SO_4 in occupying of NBM (**a**) and NBM-Ru (**b**) as well phase bode plots of Cu in the occupying of NBM (**c**) and NBM-Ru (**d**) at 25 °C

capacity, efficiency, stability, and degradation of materials over repeated cycles. Figures 13 and 14 present galvanostatic charge-discharge profiles for a copper electrode in 1 M sulfuric acid electrolyte. These curves compare performance in additive-free solutions against formulations containing additives, measured across current densities ranging from ± 1 to ± 30 mA·cm^{-2} (± 1, ± 3, ±5, ± 10, ±20, and ± 30 mA·cm^{-2}). As shown in the diagram, increasing the applied current density from ± 1 mA cm^{-2} to ± 30 mA cm^{-2} results in higher specific capacitance (S.C.) and greater potential difference (ΔV) for the tested electrode. The data indicates favorable charge-discharge characteristics for the electrode material, regardless of additive presence. Furthermore, consistent discharge capacity has been demonstrated across multiple current density conditions. Notably, higher applied current density consistently extends discharge duration (t_{dis}) across both additive-rich and additive-depleted electrochemical systems. It is widely understood that the energy storage capacity of copper electrodes depends critically on the efficiency with which the copper anode material interacts within the electrolyte environment. However, copper oxidation proves incompatible with anode applications in specific scenarios. Within these spent solutions, hydrogen gas naturally liberates itself across exposed surfaces. Elevating concentrations of NBM and NBM-Ru inhibits copper's inherent self-discharge kinetics, thereby enhancing discharge efficiency [64]. Figure 15 indicated change of (ΔV, *S.C.*) with current density at distinct dosages of additives for the investigated electrode in 1 M H_2SO_4.

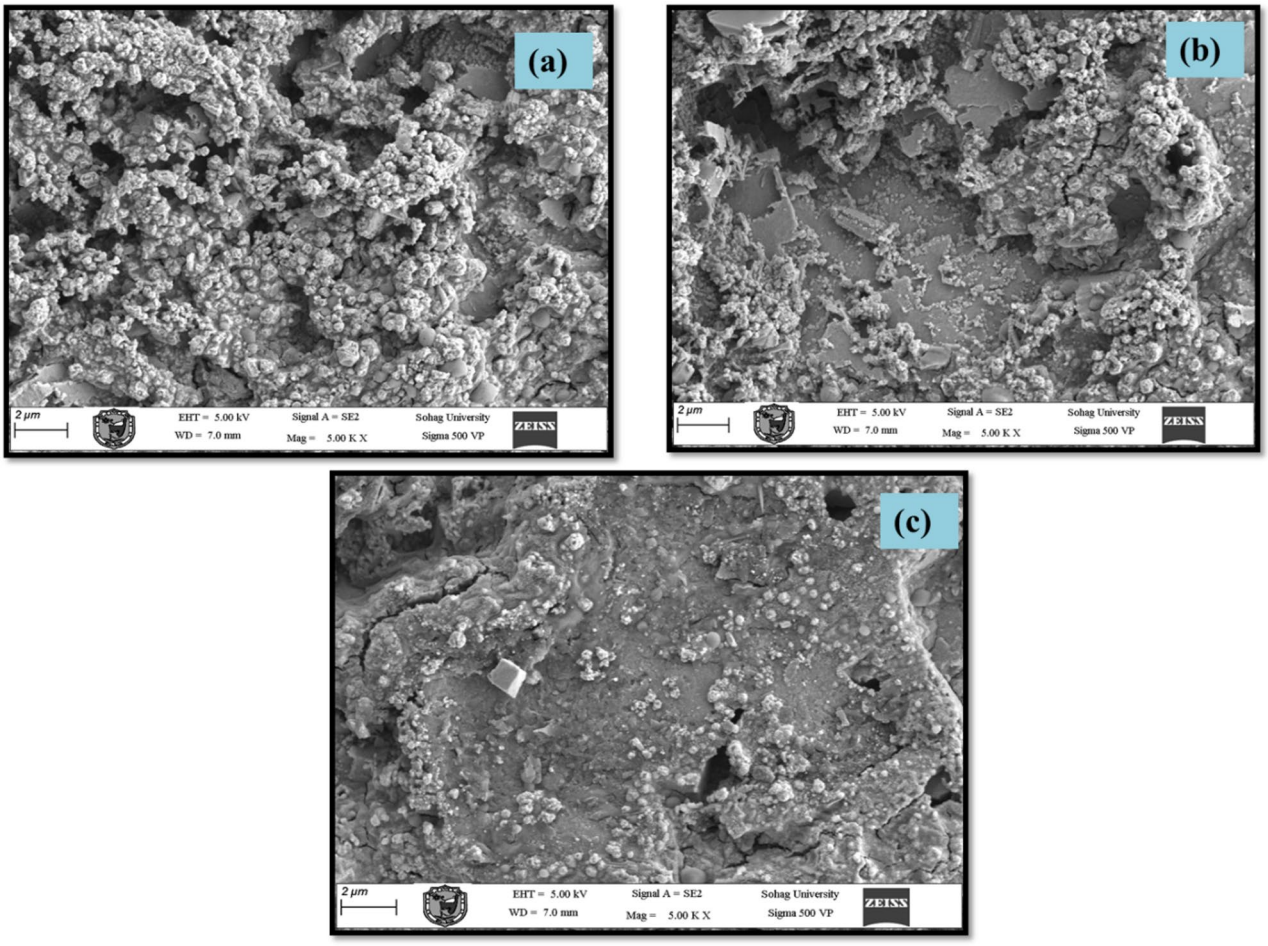


Fig. 11 Scanning electron microscope images for the oxide layers formed on Cu in 1M H_2SO_4 without additives (**a**), in presence of 1×10^{-6} M (**b**) and 1×10^{-4} M of NBM-Ru additive at magnification of ×5000

The above results exhibit the stability of the investigated electrode. It was detected that discharging time of Cu has its higher value when there is 1×10^{-4} M of NBM or NBM-Ru in 1 M H_2SO_4 manifesting that its impedance behaviors were improved confirming get impedance data. These experimental data demonstrated that energy efficiency has been improved. Finally, present data can be exhibited that adding of NBM and NBM-Ru has intelligent impact on developing performance of copper anode in acidic media. The rise in performance can be ascribed to the fact that these additives have caused the E_{corr}'s potential to shift more significantly to the negative value for the electrode. The tested electrode demonstrates reduced corrosion, extended discharge duration, and increased capacitance when exposed to our newly synthesized ligand and its corresponding complex.

The improvement in charge–discharge performance in the presence of corrosion inhibitors can be primarily attributed to their ability to stabilize the electrode/electrolyte interface and suppress undesirable side reactions. Corrosion inhibitors typically adsorb onto the electrode surface via heteroatoms (e.g., N, and O) and π-electron systems, forming a protective and compact film. This adsorbed layer effectively reduces direct exposure of the electrode material to the aggressive electrolyte, thereby minimizing metal dissolution and structural degradation during repeated electrochemical cycling. Such surface protection has been widely reported to play a critical role in maintaining electrochemical stability and prolonging electrode lifespan [65]. In addition to surface protection, corrosion inhibitors significantly influence interfacial charge transfer processes. The formation of an adsorbed inhibitor layer can regulate electron transfer kinetics by decreasing interfacial resistance and preventing the accumulation of insulating corrosion products. This facilitates more efficient electron transport and enhances the reversibility of redox reactions during charge–discharge cycles. Moreover, the suppression of parasitic reactions, such as hydrogen evolution and electrolyte decomposition, leads to improved coulombic efficiency and reduced polarization effects. These combined effects ultimately result in enhanced specific capacity and improved

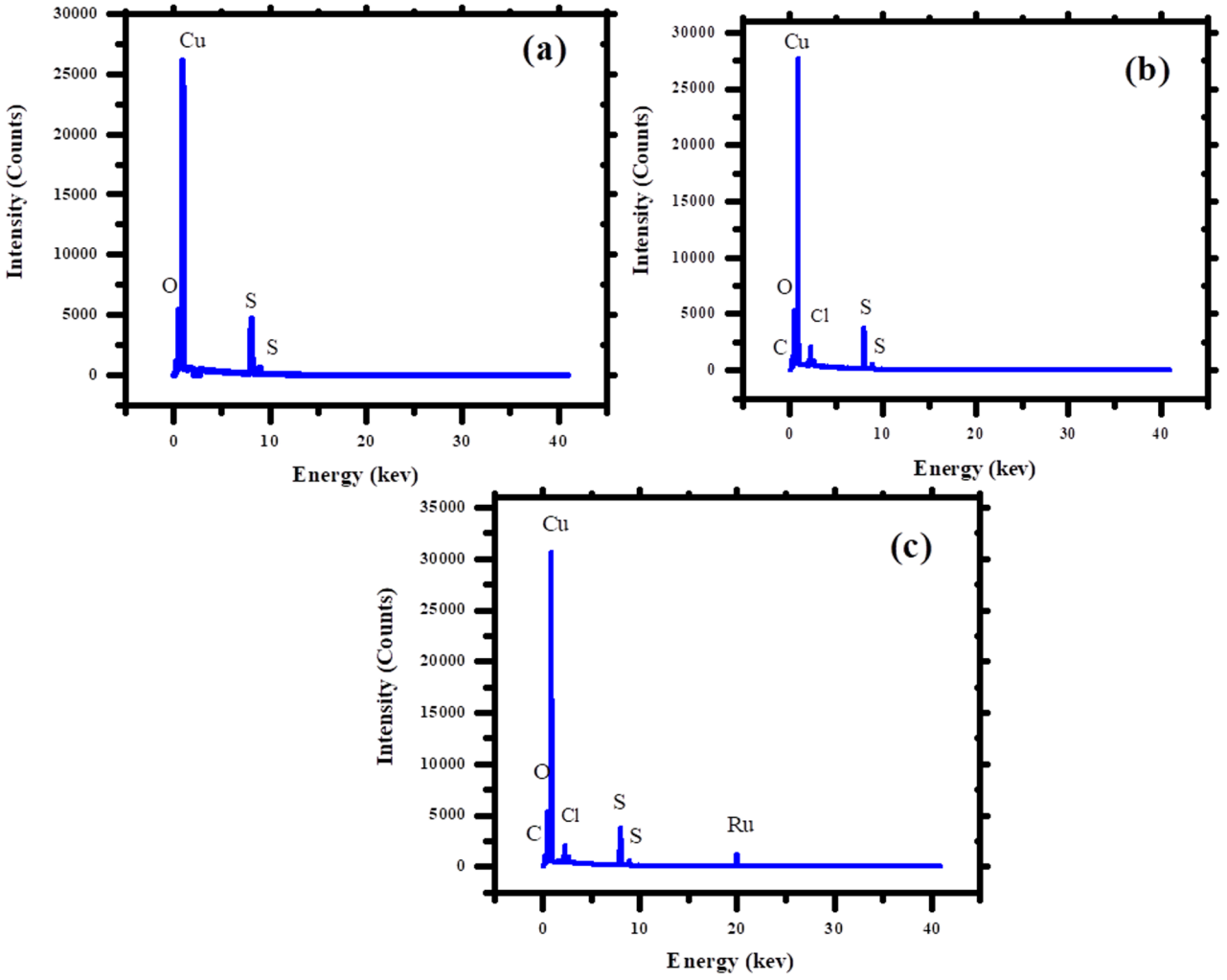


Fig. 12 EDAX analysis for the oxide layers formed on Cu after Tafel experiments in 1M H_2SO_4 without additives (**a**), containing 1×10^{-6} M (**b**) and 1×10^{-4} M (**c**)

cycling stability [66]. Furthermore, corrosion inhibitors contribute to preserving the integrity of the electrode microstructure by preventing surface pitting and crack formation. This structural stability ensures sustained ion diffusion pathways and consistent electroactive surface area throughout prolonged cycling. In systems where nanostructured or porous electrodes are employed, such stabilization is particularly important, as it prevents pore blockage and maintains electrolyte accessibility. Consequently, the presence of corrosion inhibitors supports long-term electrochemical durability and reliable charge–discharge behavior [67].

The effective inhibition of copper corrode represents a critical enabling technology for the advancement of electrochemical energy storage systems. As super capacitors and batteries continue to push toward higher energy densities, power outputs, and longer lifespans, the development of sophisticated corrosion protection strategies becomes increasingly important. Success in this field requires interdisciplinary collaboration combining electrochemistry, materials science, surface engineering, and computational modeling to develop comprehensive solutions that address the complex challenges posed by copper corrosion in these demanding applications. The future of copper corrosion inhibition in energy storage lies in the development of smart, adaptive systems that can provide targeted protection while maintaining the exceptional electrical and thermal properties that make copper indispensable in these applications. Through continued research and innovation in this field, it will be possible to realize the full potential of copper-based components in next-generation energy storage technologies. Comparison has been carried out between the specific capacitance of Cu in the acidic medium and other data obtained for Cu electrodes in literature. This comparison has been listed in supporting information (Table S4) to outline the enhancement occurred in energy storage features in presence of novel prepared additives. It is clear

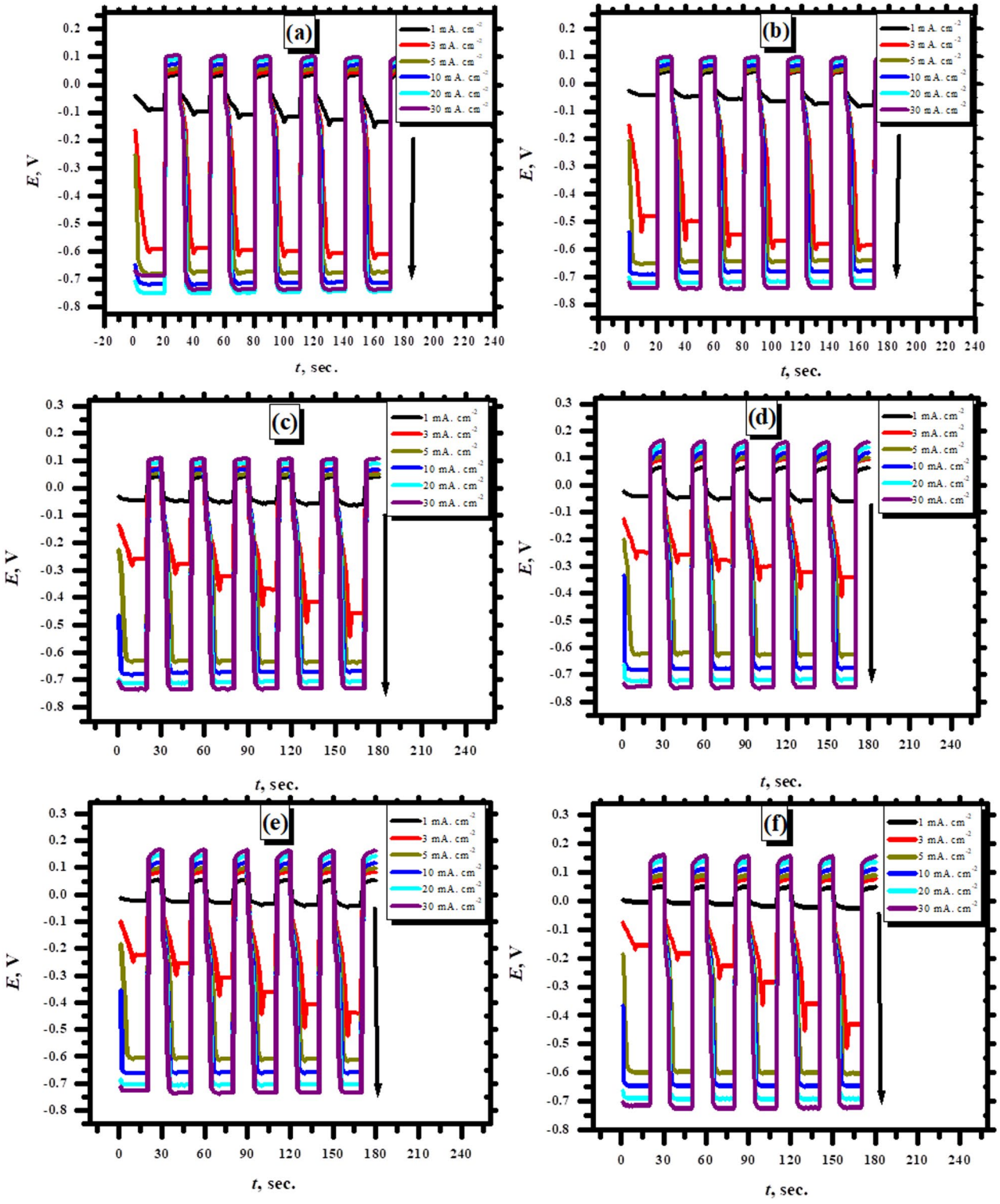


Fig. 13 Charge discharge cycling curves for Cu in 1M H_2SO_4 containing various dosages of NBM additive at applied different current densities at 25 °C

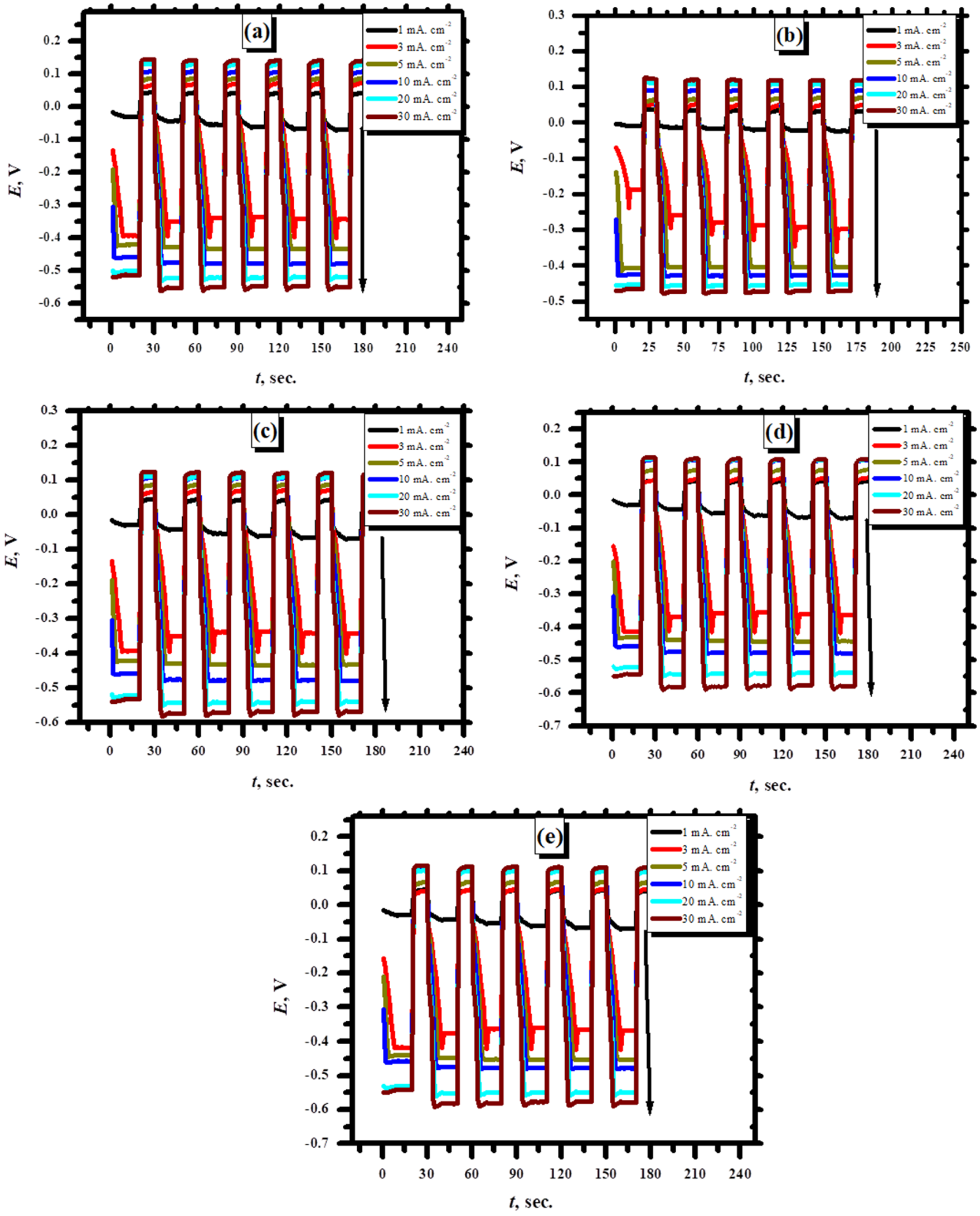


Fig. 14 Charge discharge cycling curves of Cu in 1 M H_2SO_4 containing various dosages of NBM-Ru at applied different current densities at 25 °C

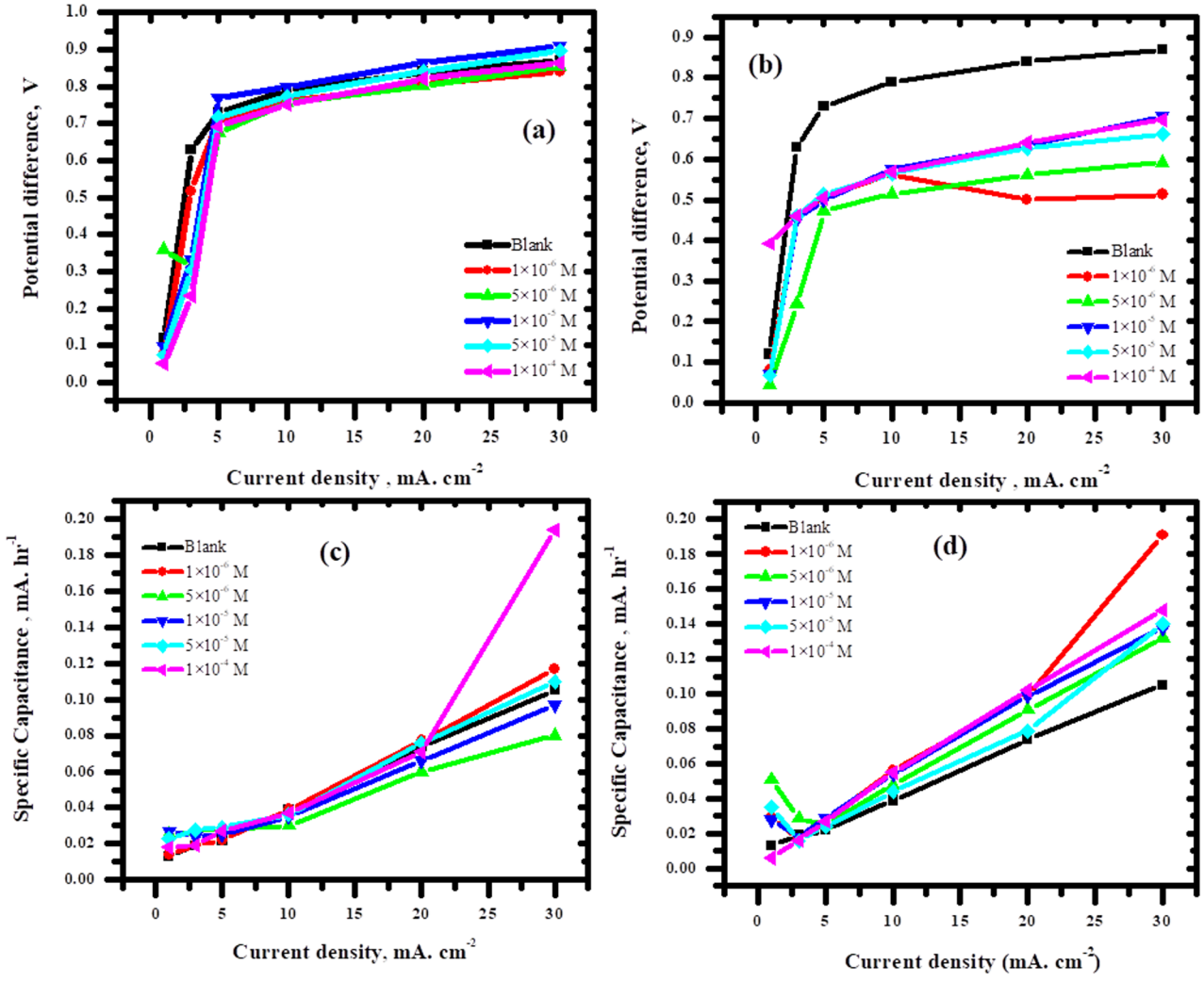


Fig. 15 Relation between potential difference of Cu electrode and current density at distinct dosages of NBM (**a**), NBM-Ru (**b**) and variation of specific capacitance with current density at distinct dosages of NBM (**c**) and NBM-Ru (**d**)

Table 6 Results of activity index (%) for antimicrobial assay of the prepared NBM Schiff base ligand and its NBM-Ru complex

Compound	Activity index (%)					
	Bacteria			Fungi		
	E. coli	S. Marcescence	M. Luteus	F. oxysporum	C. albicans	A. flavus
NBM	31.20	39.25	39.19	33.97	29.41	36.76
NBM-Ru	96.80	97.91	98.31	97.31	97.78	97.83

that specific capacitance has reached 807 and 1340 F/g in 1 M sulphuric acid solution containing NBM andNBM-Ru respectively which are higher than other S.C values of Cu electrode in presence of other additives in literature [68–71].

Biological activity

Antimicrobial

The antimicrobial performance of NBM-ligand metal complexes was rigorously evaluated against selected microbial strains: bacterial species *E. coli*, *S. marcescens*, and *M. luteus*, alongside fungal pathogens *F. oxysporum*, *C. albicans*, and *A. flavus*. Minimum inhibitory concentration (MIC) values—a key metric for antimicrobial efficacy were documented in Tables 6 and 7 and visualized in Figs. 16 and 17. Reference standards ofloxacin (bacteria) and fluconazole (fungi) enabled comparative analysis. Bioactivity of these complexes extended beyond simple chelation principles. Pharmacokinetic and steric influences—including molecular geometry, lipid solubility, coordination sites, metal ion properties, and ligand architecture collectively governed cellular membrane

Table 7 Minimum inhibition zone (MIC) for antimicrobial assay of the prepared NBM Schiff base ligand and its NBM-Ru complex

Compound	(MIC) minimum Inhibition concentration µg/ mL					
	Bacteria			Fungi		
	E. coli	S. Marcescence	M. Luteus	F. oxysporum	C. albicans	A. flavus
NBM	8.25	7.75	6.75	6.75	6.00	7.00
NBM-Ru	3.00	2.25	1.50	2.50	2.00	2.75
Ofloxacin	2.50	1.75	1.25			
Fluconazol				2.25	1.50	2.00

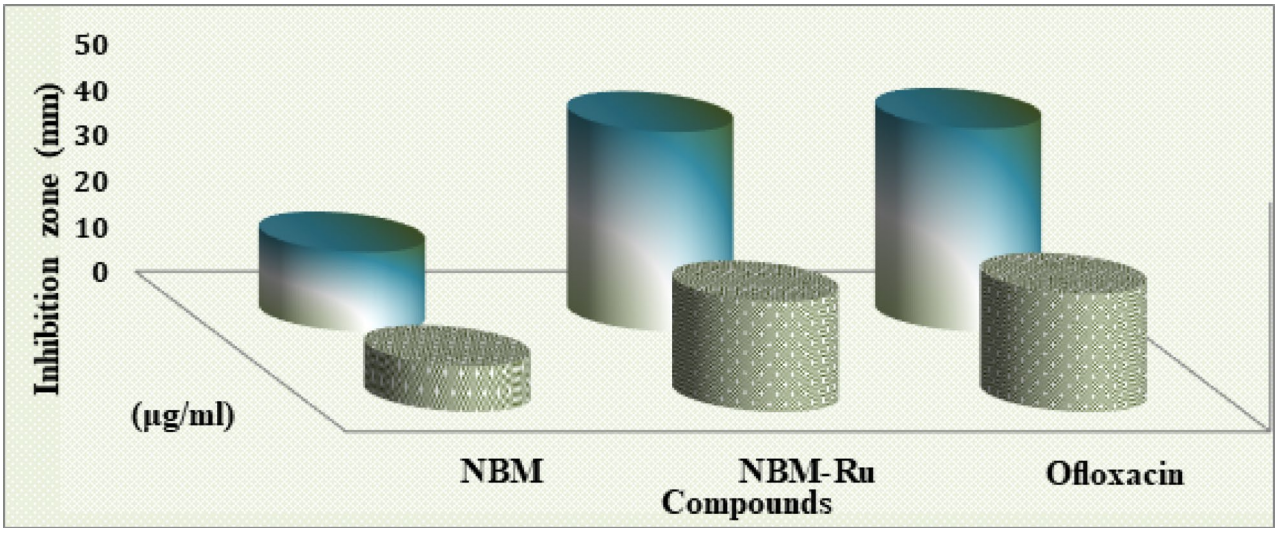


Fig. 16 Antibacterial activity for the NBM compounds under inspection against *M. luteus* bacteria

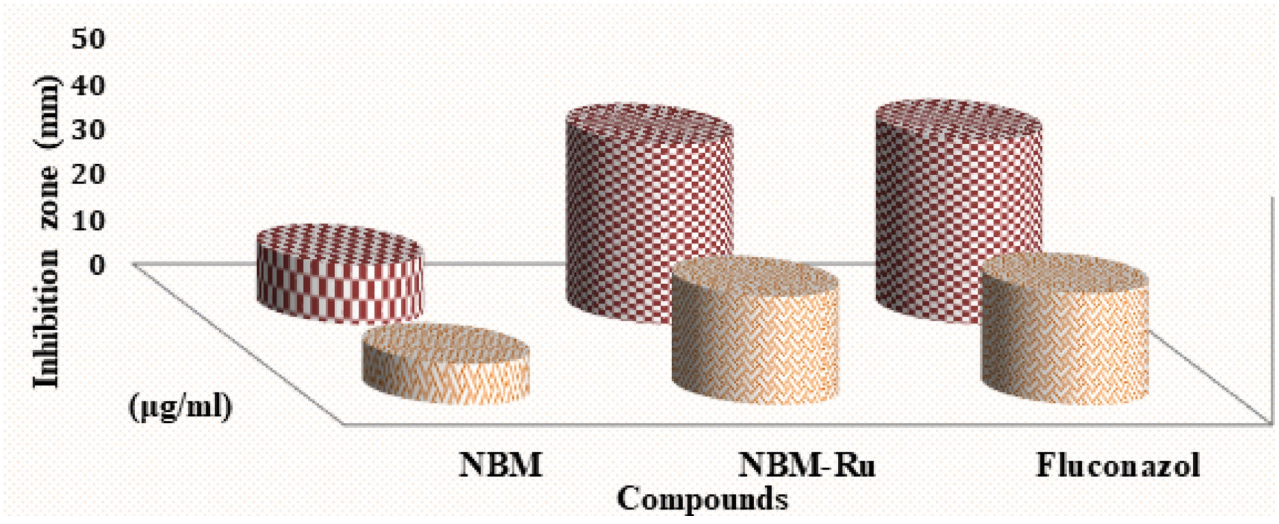


Fig. 17 Antifungal activity for the NBM compounds under inspection against *C. albicans* fungi

penetration and biomolecular interactions. Such factors critically determine compound-biosystem engagement, as established in prior research [72]. Notably, the NBM-Ru complex demonstrated superior antimicrobial potency, attributable to its pronounced surface toxicity, structural precision, and strong redox behavior. These traits likely disrupt essential intracellular components or membrane integrity [73]. Supporting evidence emerged from significant inhibition zones, elevated activity indices (Tables 6 and 7), and low MIC readings. Chelation alone proved insufficient to guarantee enhanced bioactivity. The spatial configuration of nitrogen donors around the central metal ion could either potentiate or diminish effects relative to unbound ligands [74]. This underscores

the decisive roles of ligand stereochemistry and metal coordination geometry in antimicrobial outcomes [75]. The ligand's NBM and its NBM-Ru metal chelate demonstrated varying levels of antimicrobial activity, which can be quantitatively evaluated using the following formula for the activity index (A):

$$\text{Antimicrobial activity index (A)} = \frac{\text{Inhibition zone of compound (mm)}}{\text{Inhibition zone of standard drug (mm)}} \times 100$$

The NBM-Ru metal complex demonstrated notably higher MIC values against *Micrococcus luteus* compared to other bacterial strains tested. In contrast, *Candida albicans* exhibited the most limited growth inhibition zones across all microorganisms evaluated (Tables 2S and 3S). Bioactivity assessment revealed the following potency sequence: NBM-Ru complex > NBM ligand alone. These differential effects likely stem from distinct interactions between metallic ions and species specific microbial membrane characteristics. The antimicrobial mechanism of NBM-Ru consequently represents a multifaceted relationship involving ligand architecture, coordinated metal properties, and target cell envelope dynamics. This underscores the critical importance of strategic ligand engineering and metal ion pairing when developing novel antimicrobial compounds.

The antimicrobial activity of the synthesized ligand and Ru(III) complex was quantitatively compared with standard antibiotics, and statistical analysis (one-way ANOVA, $p < 0.05$) confirms that the compounds exhibit comparable or superior activity, particularly against *M. luteus* and *C. albicans* (Tables 2S and 3S).

The NBM-Ru complex dissolves readily in water, unlocking its potential as a potent antimicrobial agent. This solubility transforms how the compound interacts with bacterial cells—instead of clumping or remaining inert, it penetrates cell membranes efficiently, disrupting critical processes from within. Studies reveal that water-soluble NBM-Ru targets enzymes essential for bacterial survival, binding to them with precision like a key fitting into a lock. This interaction halts metabolic pathways, starving pathogens of energy and halting their replication. Unlike hydrophobic counterparts that struggle to reach their targets, the dissolved complex spreads uniformly through aqueous environments, ensuring consistent contact with microbes. Laboratory tests against resistant strains like *M. luteus* bacteria show rapid cell wall degradation within hours. Researchers attribute this "smart" toxicity to the ruthenium core's electron configuration, which activates only in the presence of bacterial-specific proteins. Further, solubility enhances bioavailability in biological systems. In simulated infection models, the complex circulates effectively through fluids, accumulating at infection sites without precipitation. This mobility, combined with its mechanism of action, suggests promise for treating deep-seated infections where traditional antibiotics fail. Ongoing work explores how slight tweaks to its molecular structure could amplify these effects, potentially ushering in a new class of water-driven antimicrobial therapies.

In silico docking simulations

To complement the experimental evaluation of antibacterial and antifungal activities, molecular docking simulations were performed for NBM and its Ru(III) complex (NBM-Ru). The docking calculations provide molecular-level insight into the binding mode of these inhibitors with bacterial and fungal protein targets, thereby validating the observed biological activities. The binding affinity values revealed that the Ru(III) complex exhibited stronger interactions with both microbial targets compared to the free ligand. NBM-Ru displayed binding scores of -7.17 kcal/mol and – 8.86 kcal/mol against the bacterial and fungal targets, respectively, whereas NBM showed slightly lower affinities of -6.94 and – 8.46 kcal/mol. These results are fully consistent with the experimental assays, in which NBM-Ru demonstrated superior antibacterial and antifungal activity. Furthermore, the docking trend parallels the electronic structure results obtained from DFT insights, where the narrower HOMO-LUMO gap of the Ru(III) complex suggested greater chemical reactivity and enhanced interaction capability. The detailed interaction profile highlights the molecular determinants underlying this enhanced activity. In the case of the bacterial target, NBM-Ru forms multiple stabilizing interactions (Fig. 18). Hydrogen bonds were observed with ASN188, TYR67, LYS22, and LYS66, which contribute to the specificity and stability of the ligand-protein complex. Hydrophobic contacts with PRO190 further reinforce the binding, while additional van der Waals interactions with residues such as ALA187, MET189, LYS109, and GLU111 provide a complementary stabilizing network. This combination of directional hydrogen bonds and non-covalent contacts facilitates a snug fit within the bacterial active site, accounting for the favorable binding energy and enhanced inhibitory potential of the complex. Similarly, docking with the fungal protein target revealed an even stronger interaction pattern for the Ru(III) complex (Fig. 18). Hydrogen bonds were identified with PRO230 and LYS90, while hydrophobic contacts were established with LEU87, VAL234, and ILE231. Importantly, extensive van der Waals interactions were observed with a range of residues, including MET92, PHE380, TYR64, HIS377, PHE233, LEU88, GLY65, and SER506. The multiplicity and diversity of these contacts indicate a broad and stable engagement of the Ru(III) complex within the fungal binding pocket. The reliability of the docking protocol

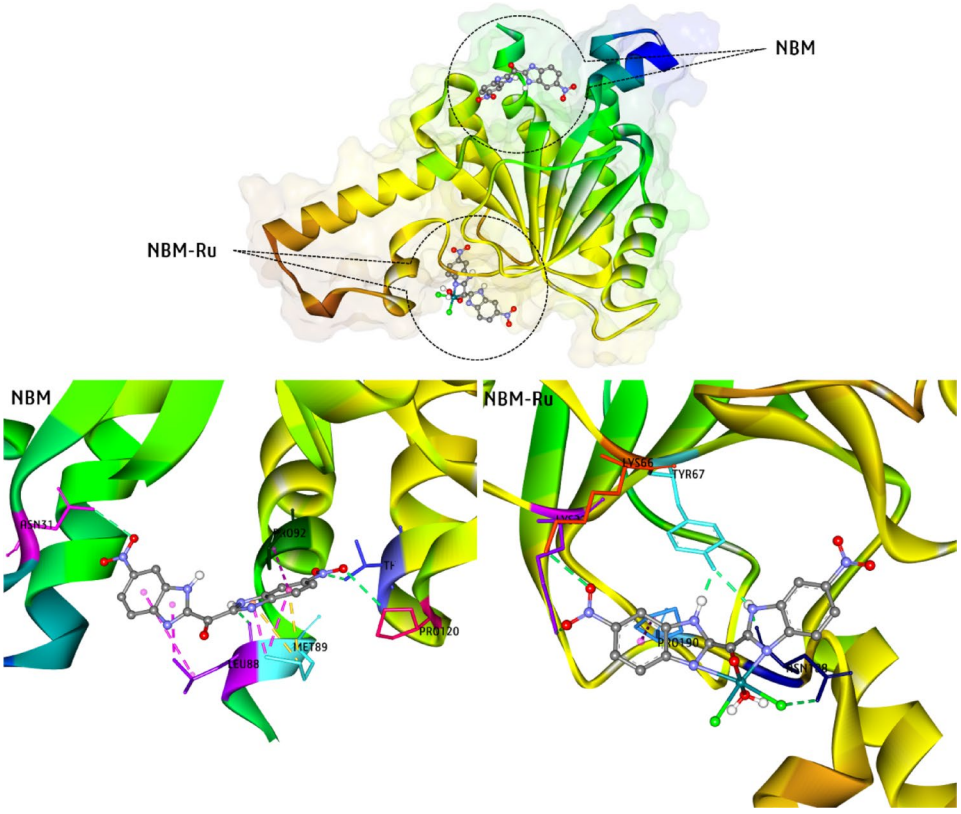


Fig. 18 Docking simulation of NBM and NBM-Ru against *Micrococcus luteus* target

was validated by calculating the root-mean-square deviation (RMSD). The obtained RMSD values for the studied systems were found to be within acceptable limits (below 2.0 Å), confirming the accuracy and reproducibility of the docking procedure. Such low RMSD values indicate that the docking protocol is capable of reliably reproducing the binding orientation within the active site.

These computational findings support two key conclusions. First, they provide mechanistic evidence that the enhanced biological activity of the Ru(III) complex is not solely due to its intrinsic reactivity, but also to its ability to engage in diverse stabilizing interactions within microbial targets. Second, they establish a clear correlation between electronic structure and biological function: the reduced HOMO-LUMO gap of NBM-Ru facilitates charge redistribution and flexible binding interactions, which in turn translate into stronger docking affinities and improved antimicrobial performance. As a results, the docking results corroborate both the experimental bioassay data and the theoretical predictions, underscoring the Ru(III) complex as a promising candidate with potent antibacterial and antifungal potential. The dual reinforcement from quantum chemical descriptors and docking studies strengthens the case for considering Ru(III)-based systems as efficient multifunctional agents.

The in silico analysis plays a crucial role in providing molecular-level insight into the structural, electronic, and interaction properties of the studied systems, which cannot be directly obtained from experimental techniques alone. In this work, DFT calculations were used to elucidate the coordination behavior, electronic structure, and reactivity descriptors of NBM and its Ru(III) complex, while molecular docking simulations were employed to predict and rationalize their biological activity against microbial targets. Importantly, the computational results show strong agreement with the experimental findings. The DFT analysis revealed that the Ru(III) complex possesses a significantly lower HOMO–LUMO energy gap, higher softness, and enhanced electron-donating ability compared to the free ligand, indicating greater chemical reactivity and stronger interaction capability. These features directly correlate with the experimental anticorrosion results, where the Ru(III) complex exhibited superior inhibition efficiency due to its improved adsorption on the metal surface. Similarly, the molecular docking results are consistent with the antimicrobial assays. The Ru(III) complex demonstrated higher binding affinities toward both bacterial and fungal targets compared to the free ligand, which aligns with its experimentally observed enhanced antibacterial and antifungal activities. The docking study further provides a mechanistic explanation

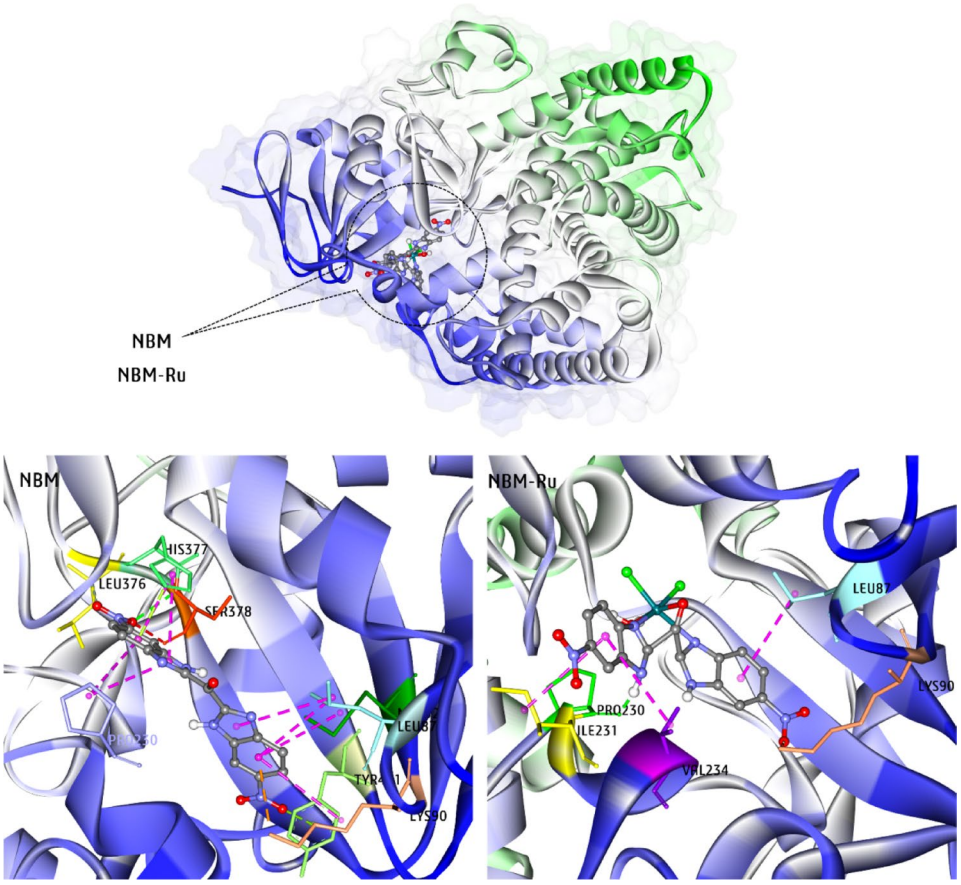


Fig. 19 Docking simulation of NBM and NBM-Ru against *Candida albicans* target

by revealing the formation of multiple stabilizing interactions, including hydrogen bonding, hydrophobic contacts, and van der Waals interactions within the active sites of the target proteins. Therefore, the in silico investigations not only support and validate the experimental observations but also offer a deeper understanding of the structure–activity relationship. The combined theoretical and experimental approach strengthens the reliability of the results and confirms that the improved performance of the Ru(III) complex arises from its optimized electronic properties and stronger interaction potential.

Conclusion

A novel tri-dentate ligand derived from bis-(6-nitro-1 H-benzimidazol-2-yl)-methanone was synthesized and demonstrated effective coordination with Ru^{III} ion. Comprehensive characterization using physicochemical techniques including elemental analysis (CHN), NMR, and electronic absorption spectroscopy confirmed molecular structures and established a consistent 1:1 ligand-to-metal stoichiometry. The resulting complex adopts an octahedral geometry confirmed by DFT calculation. Multiple amounts of NBM as well NBM-Ru additives are utilized as inhibitors for Cu in acidic media. It is discovered that corrosion current densities of Cu were declined in the presence of different inhibitor concentrations by utilizing potentiodynamic polarization method. This behavior is clear in case of utilizing both NBM as well as NBM-Ru. For copper, inhibitory effect values were 97% and 98.9% in presence of 1×10^{-6} M of NBM and 1×10^{-4} M NBM-Ru at temperature of 25 °C, respectively. EIS studies have been conducted for the examined electrode in acidic media with varying additive amounts present. According to Nyquist plots, charge transfer resistance progressively has been increased in the presence of the additives. Furthermore, Cu's charge transfer resistance values are larger when NBM-Ru is present in different concentrations than when NBM is present under the same circumstances and concentrations. This result is consistent with information obtained from potentiodynamic polarization studies using Tafel plots. Galvanostatic charge-discharge cycling curves at applied various current densities are conducted to study the influence of each additive on charge-discharge features of Cu in the acidic circumstances. It has been found that addition of 1×10^{-6} and 1×10^{-4} M of NBM and

NBM-Ru give enhanced specific capacitance of copper at applied current density of ± 30 $mA.cm^{-2}$ in acidic conditions. The charge-discharge data demonstrated improved stability in the electrode under study. This enhancement directly correlates with optimized impedance characteristics, validating the impedance measurements obtained. Furthermore, the potential for eco-friendly formulations makes these additives an attractive approach to conventional corrosion inhibitors, contributing to sustainable material protection strategies. To evaluate therapeutic prospects, antimicrobial potential was assessed. Results indicated that the NBM-Ru complex exhibits significant inhibitory activity against diverse bacterial and fungal pathogens, suggesting its viability as a candidate for novel chemotherapeutic development. Molecular docking simulation was applied to confirmed the biological activity of the investigated NBM ligand and its NBMRu complex.

Supplementary Information

The online version contains supplementary material available at https://doi.org/10.1186/s13065-026-01824-y.

Supplementary Material 1

Author contributions

All authors have contributed equally to the study.

Funding

Funding is not available.

Data availability

All data are given in the manuscript.

Declarations

Competing interests

The authors declare no competing interests.

Author details

[1]Department of Chemistry, Faculty of Science, Sohag University, Sohag 82524, Egypt
[2]Department of Basic Pharmaceutical Sciences, Faculty of Pharmacy, Suleyman Demirel University, Isparta, Türkiye
[3]Faculty of Engineering and Natural Sciences, Bahcesehir University, Istanbul, Türkiye
[4]Department of Chemistry, College of Science, Taibah University, Al- Madinah Al-Munawara 42353, Saudi Arabia
[5]Department of Chemistry, College of Science, Imam Mohammad Ibn Saud Islamic University (IMSIU), Riyadh 11623, Saudi Arabia

Received: 10 January 2026 / Accepted: 30 April 2026
Published online: 11 May 2026

References

1. Salaheldeen M, Thomas Nady A, Eskander M, Fathalla V, Zhukova JM, Blanco J, Gonzalez A, Zhukov AM, Abu-Dief. Empowering the Future: Cutting-Edge Developments in Supercapacitor Technology for Enhanced Energy Storage. Batteries. 2025;11(6):232.
2. Mohamed Salaheldeen, Ahmed M, Abu-Dief. Tarek El-Dabea, Functionalization of Nanomaterials for Energy Storage and Hydrogen Production Applications. Materials. 2025;18(4):768.
3. (a)Tan Bochuan, Ren H, Liu Y, Xin Li R, Wang J, Sun XC, Dai Q, Guo L, Liu H, Mohammad K, Al-Sadoon, Insight into the anti-corrosion performance of crop waste as a degradable corrosion inhibitor for copper in sulfuric acid medium, Industrial Crops and Products 222(2024) 119654 ;(b) Mahmoud GA, Amal M, Abdel-karim SM, Saleh, Amin A, El-Meligi AA. El-Rashedy, Corrosion inhibition of copper alloy of archaeological artifacts in chloride salt solution using Aloe vera green inhibito, Journal of Alloys and Compounds. (2025);1010:177540.
4. (a)Chu Q, Zhao S, Liu Z, Zhang X, Recent advances in carbon dots as powerful ecofriendly corrosion inhibitors for copper and its alloy, Materials Today Sustainability 26,(2024) 100706; (b) Ahmed MA. Sherif Amin, Ashraf A. Mohamed, Current and emerging trends of inorganic, organic and eco-friendly corrosion inhibitors, (Review Article) RSC Adv., 2024, 14, 31877–31920.
5. Fatima Janoub A, Chraka J, Kassout NB, Seddik A, Ghajjou F, Chaouket D, Bouchta K, Draoui M, Benmessaoud. Ihssane Raissouni, Innovative Characterization of Coffee Waste Extracts and Their Derivatives as Efficient Ecological Corrosion Inhibitors for Copper Alloy in 3% NaCl: Phytochemical Investigations, Electrochemical Explorations. Morphological Assessment and New Computational Methodology. (2024);10:95.
6. Jabbar AH, Kamona SMH, Abbood SK, Kh T, Hussein, Dahlia N, Al-Saidi. Safaa Mustafa Hameed, Rashid Abdul Kareem Rashid, Hussein Abdullah Abbas, Mustafa M. Kadhim, The effective and sustainable application of a green amino acid-based corrosion Inhibitor for Cu metal. Chem Phys Impact. 2023;7:100316.
7. Kebede W, Shinato. Abraham Amenay Zewde and Ying Jin, Corrosion protection of copper and copper alloys in different corrosive medium using environmentally friendly corrosion inhibitors. Corros Rev. 2020;38(2):101–9.
8. Amal M, Abdel-karim HM, Hussien S, Shahen, Omnia AA, El-Shamy IM, Ghayad NM, Saleh, Nour EA. Abd El-Sattar, Green synthesis of novel bis structure of (Carbamothioyl) oxalamide derivatives as corrosion inhibitors for copper in 3.5% NaCl; experimental and theoretical investigation. J Mol Struct. 2024;1295:136597.
9. Cheng Xu B, Tan S, Zhang A, Li W. Corrosion inhibition of copper in sulfuric acid by Leonurus japonicus Houtt. extract as a green corrosion inhibitor: Combination of experimental and theoretical research. J Taiwan Inst Chem Engineers. (2022);139:104532.
10. Dahmani K, Galai M, Ouakki M, Amr Elgendy, EzZriouli R, Lachhab R, Briche S, Cherkaoui M. Corrosion inhibition of copper in sulfuric acid via environmentally friendly inhibitor (Myrtus Communis): Combining experimental and theoretical methods. J Mol Liq. 2022;347:117982.
11. (a)Ahmed M, Abu-Dief ES, Al-Farraj M, Abdel-Hameed N, Alahmadi M, Fathalla AYA, Alzahrani, Mashael A, Alghamdi, editors. Aly Abdou, Design and Synthesis of Tunable Schiff Base Complexes from Bis-(2-oxoindolin-3-ylidene) anthracene-9, 10-dione: Integrated Structural, Biological, and Molecular Modeling Insights, Computational Biology and Chemistry. (2026);120:108682; (b) Laila H Abdel-Rahman, Rafat M El-Khatib, Lobna AE Nassr, Ahmed M Abu-Dief, Synthesis, physicochemical studies, embryos toxicity and DNA interaction of some new Iron (II) Schiff base amino acid complexes, Journal of Molecular Structure. (2013);1040:9–18.
12. Hoda Abd El-Shafy Shilkamy, Mehran Feizi-Dehnayebi, Rafat M El-Khatib, Mona MA Alharas, Rawan Al-Faze, Ahmed M Abu-Dief, Tailored Novel Azomethine Ligand and Its Cu (II) Complex for Improving Corrosion Resistance and Charge–Discharge Performance of Ni in Acidic Media, Applied Organometallic Chemistry 39 (7), (, Abo-Dief M, El-Khatib RM. Ahmed M Abu-Dief, Enhanced corrosion protection as a sustainable approach for nickel using novel fel Salen complex: electrochemical investigation and DFT insights, Metals. (2025);15(4):403.
13. (a)Saad Shaaban, Shalabi K, Yousef TA, Abou-Krisha M, Alanazi AA, Althikrallah HA, Alaasar M, Ahmed M, Abu-Dief ASM, Al-Janabi. Promising organoselenium corrosion inhibitors for C1018-steel in hydrochloric acid environments, Journal of the Taiwan Institute of Chemical Engineers. (2024);165:105766; (b) Saad Shaaban, Kamal Shalabi, Tarek A Yousef, Ghayah M Alsulaim, Mohamed Alaasar, Ahmed M Abu-Dief, Ahmed SM Al-Janabi, Novel organoselenides as efficient corrosion inhibitors for N80 steel in a 3.5 wt% sodium chloride solution, Inorganic Chemistry Communications. (2025);172:113632.
14. Hany MA, El-Lateef AM, Abu-Dief LH, Abdel-Rahman EC, Sañudo, Núria Aliaga-Alcalde, Electrochemical and theoretical quantum approaches on the inhibition of C1018 carbon steel corrosion in acidic medium containing chloride using some newly synthesized phenolic Schiff bases compounds, Journal of Electroanalytical Chemistry 743, (, Punitha N, Ganapathi Sundaram R, Vengatesh G, Rengasamy R, editors. J. Elangovan Bis-1,2,3-triazole

derivative as an efficient corrosion inhibitor for mild steel in hydrochloric acid environment: Insights from experimental and computational analysis, Inorganic Chemistry Communications. (2023);153:110732.
15. Punitha)N, Ganapathi Sundaram R, Vijayalakshmi K, Rengasamy R, J. Elangovan Interactions and corrosion mitigation prospective of pyrazole derivative on mild steel in HCl environmentJournal of the Indian Chemical Society, 99, (, Jasim AS, Khadom AA, Rashid KH, editors. K. F. Al-Azawi Corrosion inhibition of mild steel in acidic media using organic inhibitor: Experimental and theoretical studies, Chemical Data Collections. (2022);41:100936.
16. Vengatesh G, Ganapathi Sundaram R, Punitha N, Rengasamy R, Elangovan J Menadione sodium bisulfite as an efficient anti-corrosion additive for mild steel in acid corrosion, editors. Electrochemical, surface and theoretical studies Journal of Molecular Liquids. (2024);410:125653; (b) N. Punitha, A. P. Priya,Corrosion prevention capability of 1,2,3-triazole derivative on mild steel in acidic medium: Experimental and theoretical approach, Chemical Data Collections. (2024);54:101172.
17. El-Remaily MAEAA, Eskander Thomas Nady A, Alzahrani A, Alsehli M, Al-Ghamdi K, Mughram AL, El-Hady OM, Feizi-Dehnayebi AM, Abu-Dief. Tailoring of Novel Ru (III) and Cr (III) Salen Complexes as Catalysts for a Sustainable and Green Synthesis of Dihydro-tetrazolo [1,5-a] thiazolo [4,5-d] pyrimidin-6-yl morpholine: Experimental and Theoretical Approaches. Appl Organomet Chem. 2025;39:e7879.
18. (a) Ahmed M, Abu-Dief MMA, Alharas IO, Barnawi WH, Alsaedi I, Omar SA, Abdel-Latif, Rafat M, El-Khatib, Facile synthesis, structural elucidation, non-linear optical properties and biological evaluation of some novel tetradentate azomethine complexes supported by DFT calculation and molecular docking approach, Journal of Molecular Structure. (2025);1326:141083; (b) Omar I, Eida S, Al-Farraj. Mohamed Abdel-Hameed, Maher Fathalla, Asmaa M Elmughamsi, Mashael A Alghamdi, Aly Abdou, Ahmed M Abu-Dief, Integrated experimental and theoretical investigation of VO (II), Ni (II), and Ru (III) nanocomplexes derived from a tetradentate anthraquinone ligand: Sonochemical synthesis and therapeutic assessment, Journal of Molecular Structure. (2026);1353;144779.
19. Zhang Z. Qingya Song,Yubin Jin,Yashan Feng,Jingan Li, and Kun Zhang Advances in Schiff Base and Its Coating on Metal Biomaterials—A. Rev Met. 2023;13:86.
20. Shilkamy HAE-S, Rafat M, El-Khatib M, Feizi-Dehnayebi, Mona MA, Alharas RAL-F, Abu-Dief AM. Green corrosion inhibitors for nickel in acidic media utilizing novel imine ligand and its Zn (II) metal chelate supported by DFT calculation. J Mol Liq. 2024;416:126468.
21. (a) Rawan AL-Faze, Alahmadi N, Barnawi IO, Alharas MMA, Abo-Dief HM, Abdel-Latif SA, El-Khatib RM, Ahmed M, Abu-Dief, Synergistic broad-spectrum bioactivity of some multifunctional novel Anil metal chelates: design, synthesise, nonlinear optical properties, and biomedical applications supported by DFT and molecular docking insights, Journal of Molecular Structure. (2025);1339:142390; (b) M.A. E. A. A. El-Remaily A, Eskander Thomas Nady O, Elhady D, Alhashmialameer M, Alsehli MS, Kamel M, Feizi-Dehnayebi AM. Abu-Dief., A comparative study for the efficiency of Pd (II) and Fe (III) complexes as efficient catalysts for synthesis of dihydro-7H-5-thia-hexaaza-s-indacen-6-one derivatives supported with DFT approach. Appl Organomet Chem. (2024);38(11):e7653.
22. (a) Abdel-Rahman LH, Abu-Dief AM, Moustafa H, Hamdan SK, Ni (II) and Cu (II) complexes with ONNO asymmetric tetradentate Schiff base ligand: synthesis, spectroscopic characterization, theoretical calculations, DNA interaction and antimicrobial studies, Appl. Organometal. Chem. (2017);31(2):e3555; (b) M. A. E. A. A. El-Remaily O, Elhady A, Eskander Thomas Nady KS, Mohamed AM. Abu- Dief., Development of Novel Guanidine Iron (III) Complexes as a Powerful Catalyst for the Synthesis of Tetrazolo [1, 5-a] pyrimidine by Green Protocol, Sohag Journal of Sciences. (2024);9(1):7–15.
23. Al-Shamry AA, Khalaf MM, El-Lateef HMA, Yousef TA, Mohamed GG, El-Deen KMK, Gouda M, Abu-Dief AM. Development of new azomethine metal chelates derived from isatin: DFT and pharmaceutical studies. Materials. 2022;16(1):83.
24. Alkhatib F, Hameed A, Sayqal A, Bayazeed AA, Alzahrani S, Al-Ahmed ZA, Zaky R, El-Metwaly NM. Green-synthesis and characterization for new Schiff-base complexes; spectroscopy, conductometry, Hirshfeld properties and biological assay enhanced by in-silico study. Arab J Chem. 2020;13(8):6327–40.
25. El-Remaily MAEAA, Elhady O, Abdou A, Alhashmialameer D, Eskander Thomas Nady A, Abu-Dief AM. Development of new 2-(Benzothiazol-2-ylimino)-2,3-dihydro-1H-imidazol-4-ol complexes as a robust catalysts for synthesis of thiazole 6-carbonitrile derivatives supported by DFT studies. J Mol Struct. 2023;1292:136188.
26.)(a)Frisch MJ, Trucks GW, Schlegel HB, Scuseria GE, Robb MA, Cheeseman JR, Scalmani G, Barone V, Mennucci B, Petersson GA, Gaussian 09, Revision D. 01, Gaussian, Inc., Wallingford CT (2009);(b) Abdel-Baset M, Soliman, Abdel-Mawgoud M, Abdel-Mawgoud. Walaa M Abd El–Raheem, Ahmed M Abu-Dief, Aly Abdou, New Octahedral Co (II)/Ni (II) and Square-Pyramidal VO (II) complexes derived from Azo-Schiff-base ligand: Synthesis, Spectroscopic, DFT, Molecular docking, and Biological Profiling Correlation, Journal of Molecular Structure. (2026);1366:146114.
27. Garrett M, Huey R, Lindstrom W, Sanner MF, Belew RK, Goodsell DS, Olson AJ. AutoDock4 and AutoDockTools4: Automated docking with selective receptor flexibility. J Comp Chem. 2009;30:2785–91.
28. MGL Tools. 1.5. 6 (ADT)/MGL Tools 1. 6.; The Scripps Research Institute: La Jolla, CA, USA, 2016.
29. (a) Finn RK, Theory of agar diffusion methods for bioassay, Anal. Chem. 31 (1957) 975. (b) Eida S, Al-Farraj SK, Alharbi BH, Asghar MA, Alghamdi AM, Abu-Dief. Molecular, Stochiometric, stability and biological investigations of novel multifunctional Salen metal chelates: from synthesis to therapeutic potential supported by theoretical approaches, Applied Organometallic Chemistry (2025);39(8):e70273.
30. (a) Osowole AA, Kempe R, Schobert R, Synthesis, spectral, thermal, in-vitro antibacterial and anticancer activities of some metal (II) complexes of 3-(-1-(4-methoxy-6-methyl)-2-pyrimidinylimino) methyl-2-napthol, Int. Res. J. Pure Appl. Chem. (2012);2:105. (b) Khulood A. Abu Al-Ola, Hamed AM, Feizi-Dehnayebi M, Eskander RA, Ahmed M, Abu-Dief. Design, Synthesis, Physicochemical Characterization, and Prospective Pharmaceutical Applications of Novel Tetra-Dentate Salen Complexes: DFT and Molecular Docking Insights, Applied Organometallic Chemistry. (2025);39(7):e70269.
31. Khalaf Al-Ghamdi AM, Hamed MA, Ibrahem SK, Alharbi KA, Abu Al-Ola MS, Amin, Thomas Nady A, Eskander, Samir A. Abdel-Latiff , AMAbu-Dief. A robust synthesis, physicochemical characterization, Stability determination and potential biomedical applications of novel Salen complexes supported by theoretical approaches. J Mol Struct. 2025;1336:142060.
32. El-Sherif AA. Synthesis, Spectroscopic Characterization and Biological Activity on Newly Synthesized Copper(II) and Nickel(II) Complexes Incorporating Bidentate Oxygen–Nitrogen Hydrazone Ligands. Inorg Chim Acta. 2009;362:4991–5000.
33. (a) Al-Hazmi GAA, Abou-Melha KS, El-Metwaly NM, Althagafi I, Shaaban F, Zaki R, Green Synthesis Approach for Fe (III), Cu (II), Zn (II) and Ni (II)-Schiff Base Complexes, Spectral, Conformational, MOE-Docking and Biological Studies, Applied Organometallic Chemistry. (2020);34:e5403; (b) Omar I, Mona MA, Alharas, Mehran Feizi-Dehnayebi, Sultan K Alharbi, Hala M Abo-Dief, Hamza A, Qasem, Rafat M, El-Khatib, Ahmed M, Abu-Dief. Design, Synthesis, Physico-Chemical Characterization, Stability Determination, and Biomedical Applications of Some Novel Tetra-Dentate Imine Metal Chelates Supported by Theoretical Approaches: Bridging Coordination Chemistry and Life Sciences, Applied Organometallic Chemistry. (2025);39(3):e70056.
34. Emara AAA. Structural, Spectral and Biological Studies of Binuclear Tetradentate Metal Complexes of N3O Schiff Base Ligand Synthesized From 4,6-Diacetylresorcinol and Diethylenetriamine. Spectrochimica Acta A. 2010;77:117–25.
35. Abdel-Rahman LH, Abu-Dief AM, Atlam FM, et al. Chemical, Physical, and Biological Properties of Pd(II), V(IV)O, and Ag(I) Complexes of N3 Tridentate Pyridine-Based Schiff Base Ligand. J Coord Chem. 2020;73(23):3150–73.
36. El-Remaily MAEAA, Elhady O, Alzubi MSH, Eskander Thomas Nady A, El Hamd MA, Al-Ghamdi K, Abu-Dief AM. Development of new thiazole-guanidine complexes as rapid and recoverable catalysts for the synthesis of 6-piperidin-dihydro-thia-hexaaza-s-indacene derivatives supported by DFT studies. Appl Organomet Chem. 2024;38(6):e7454.
37. (a)Tofq DI, Hassan HQ, Abdalkarim KA, Preparation of a novel Mixed-Ligand divalent metal complexes from solvent free Synthesized Schiff base derived from 2, 6-Diaminopyridine with cinnamaldehyde and 2, 2′-Bipyridine: Characterization and antibacterial activities, Arab. J. Chem. 2021;14:103429–103442; (b) Rahman LHA, Abu-Dief AM, editors. S. Kamel Hamdan, A. Abdou Seleem, Nano structure Iron (II) and Copper (II) Schiff base complexes of a NNO-tridentate ligand as new antibiotic agents: spectral, thermal behaviors and DNA binding ability, Int. J. Nano Chem. 2015;1(2):65–77.
38. (a)Liu YT, Lian GD, Yin DW, Su BJ, Synthesis, characterization and biological activity of ferrocene-based Schiff base ligands and their metal (II) complexes, Spectrochimica Acta Part A: Molecular and Biomolecular Spectroscopy. 2013;100:131–137; (b) El-Kasaby RA, Eida S, Al-Farraj A, Abdou AM, Abu-Dief. Synthesis, spectral analysis, physicochemical investigation and biomedical potential of some novel Cu (II), Ru (III) and VO (II) complexes with

anthraquinone-based Schiff base supported by DFT and molecular docking insights, Journal of Molecular Structure. 2025;1345:143010.
39. (a)Surati KR, Thaker BT, Synthesis, Spectral, Crystallography and Thermal Investigations of Novel Schiff Base Complexes of Manganese (III) Derived from Heterocyclic β-Diketone with Aromatic and Aliphatic Diamine, Spectrochimica Acta. Part A, Molecular and Biomolecular Spectroscopy. 2010;75:235. (b) Qasem HA, Sayed FN, Feizi M-D ehnayebi et al., editors. Development of Tripodal Imine Metal Chelates: Synthesis, Physicochemical Inspection, Theoretical Studies and Biomedical Evaluation, Inorganic Chemistry Communications. 2024;162:112248.
40. Abdel-Rahman LH, Abu-Dief AM, Basha M, AbdelMawgoud AAH. Three Novel Ni (II), VO (II) and Cr (III) Mononuclear Complexes Encompassing Potentially Tridentate Imine Ligand: Synthesis, Structural Characterization, DNA Interaction, Antimicrobial Evaluation and Anticancer Activity. Appl Organomet Chem. 2017;31:11.
41. (a)Vadivel T, Kulathooran S, Chandrasekaran S, Ilayaraja S, Benjamin R, editors. Electrochemical studies of Ruthenium (III) complexes derived from chitosan Schiff base ligands. Carbohydrate Research. 2025;554:109557; (b) A. B. P. Lever, Electronic spectra of some transition metal complexes: Derivation of Dq and B J. Chem. Educ. 1968;45(11):711.
42. Erik MJ, Johansson M, Odelius S, Plogmaker M, Gorgoi S, Svensson H, Siegbahn. Håkan Rensmo, Spin–Orbit Coupling and Metal–Ligand Interactions in Fe(II), Ru(II), and Os(II) ComplexesArticle link copied. J Phys Chem C. 2010;114:10314–22.
43. (a) Ismail TMA, Saleh AA, El MA, Ghamry, Tetra-and hexadentate Schiff base ligands and their Ni (II), Cu (II) and Zn (II) complexes. Synthesis, spectral, magnetic and thermal studies**9** Spectrochim. Acta A. 2012;86:276; (b) Abdel-Rahman LH, Abu-Dief AM, Hashem NA, Seleem AA. Recent Advances in Synthesis, Characterization and Biological Activity of Nano Sized Schiff Base Amino Acid M (II) Complexes**9** Int. J. Nano Chem. 2015;1(2):79–95.
44. (a) MontazerozohoriM, MojahediJahromi S, Masoudiasl A, McArdle P, Nano Structure Zinc (II) Schiff Base Complexes of a N3- Tridentate Ligand as New Biological Active Agents: Spectral, Thermal Behaviors and Crystal Structure of Zinc Azide Complex, Spectrochimica Acta, Part A: Molecular and Biomolecular Spectroscopy. 2015;5:517. (b) Abu-Dief AM, Omran A, Omran M, Feizi-Dehnayebi, et al. editors. Fabrication, Structural Elucidation, and DFT Calculation of Some New Hydrophilic Metal Chelates Based on NN'-(1-Methyl-2-oxoindolin-3-ylidene) benzohydrazide Ligand: Pharmaceutical Studies and Molecular Docking Approach, Applied Organometallic Chemistry. 2024;38(9):e7593.
45. Hamza A, Qasem MR, Aouad, Hessah A, Al-Abdulkarim ES, Al-Farraj RMS, Attar NM, El-Metwaly AM, Abu-Dief. Tailoring of Some Novel Bis-Hydrazone Metal Chelates, Spectral Based Characterization and DFT Calculations for Pharmaceutical Applications and In-Silico Treatments for Verification. J Mol Struct. 2022;1264:133263.
46. Abu-Dief AM, Said MA, Elhady O, Alzahrani S, Aljohani FS, Eskander Thomas Nady A. M. A. E. A. A. El-Remaily., Design, structural inspection of some new metal chelates based on benzothiazol- pyrimidin-2-ylidene ligand: Biomedical studies and molecular docking approach. Inorg Chem Commun. 2023;158:111587.
47. Abu-Dief AM, Musa Said A, Elhady O, Alahmadi N, Alzahrani S, Eskander Thomas Nady A, El-Remaily MAEAA. Designing of some novel Pd(II), Ni(II) and Fe(III) complexes: Synthesis, structural elucidation, biomedical applications, DFT and docking approaches against Covid-19 . Inorganic Chemistry Communications. 2023;155:110955.
48. (a) Ejidike IP, Direm A, Parlak C, Olaleru SA, Adetunji CO, Mtunzi FM, Athar, Ata DNA gyrase inhibition by Ni (II)-Schiff base complexes via in silico molecular docking studies: Spectroscopic, DFT calculations and in vitro pharmacological assessment. Results in Chemistry. 2025;15:102219; (b) Ejidike, Ikechukwu P, Direm A, Parlak C, Adeniyi AA, Mohammad Azam, Athar Ata, Eze MO, Hollett JW, Hadley S. Clayton. Spectroscopic characterization, DFT calculations, in vitro pharmacological potentials, and molecular docking studies of N, N, O-Schiff base and its trivalent metal complexes. Chemical Physics Impact. 2024;8:100549.
49. Abu-Dief AM, Feizi-Dehnayebi M, Nafady A, Almalki MA, Ahmed M, Kassem KA, Abu Al-Ola BM, Altayeb, Laila H, Abdel-Rahman. Fabrication, structural inspection, stability studies in solution and DFT calculations of some novel complexes drived from 4-(Benzothiazol-2-yliminomethyl)-phenol ligand: Pharmaceutical applications supported by molecular docking approach. J Mol Struct. 2025;1328:141284.
50. Abu-Dief AM, Rafat M, El-Khatib, Tarek El-Dabea M, Feizi-Dehnayebi IO, Barnawi AH, Alsehli. Khalaf Al-Ghamdi, and Mahmoud Abd El Aleem Ali Ali El-Remaily. Design, preparation, physicochemical characterization, structural conformational, biological evaluation, and DNA interaction for some new benzimidazole complexes. Appl Organomet Chem. 2024;38(3):e7358.
51. (a)Ziarani GM, Lohith TN, Ghareghomi S, Panahande Z, Farsadrooh M, Majidinia M. Probing the biological activity of isatin derivatives against human lung cancer A549 cells: Cytotoxicity, CT-DNA/BSA binding, DFT/TD-DFT, topology, ADME-Tox, docking and dynamic simulations. Journal of Molecular Liquids. 2025;428:127475; (b) Jamshidi, Shokoofeh, Ali Eghbalian, Setareh Shojaei, Amir Taherkhani, and Mehran Feizi-Dehnayebi. Flavonoids as promising Akt1 inhibitors in Cancer medicine: insights from molecular docking, dynamics, DFT calculations, and in vitro validation. Cancer Reports. 2025;8(8):e70315.
52. Feizi-Dehnayebi M, Dehghanian E, Mansouri-Torshizi H. DNA/BSA binding affinity studies of new Pd (II) complex with SS and NN donor mixed ligands via experimental insight and molecular simulation: Preliminary antitumor activity, lipophilicity and DFT perspective. J Mol Liq. 2021;344:117853.
53. Hashim KM, Manoj E, Kurup MP. A novel manganese (II) bisthiocarbohydrazone complex: Crystal structures, Hirshfeld surface analysis, DFT and molecular docking study with SARS-CoV-2. J Mol Struct. 2021;1246:131125.
54. Kundu S, Feizi-Dehnayebi M, Akkoc S. Exploring the anticancer potential of novel benzimidazolium salts: synthesis, biological evaluation, DFT perspective, and docking simulation for inhibition of VEGFR2. Biochem. Biophys. Res. Commun. 2025;11:152472.
55. Sultan K, Alharbi SM, Alahmadi I, Omar MM, Khashoqji, Faizah S, Aljohani IO, Barnawi M, Fathalla SA, Abdel-Latif M, Salaheldeen, Ahmed M, Abu-Dief. Design of Quinoline-Derived Schiff Base Metal Complexes as Bioactive Drug Candidates: Structural Elucidation, Stability Determination, DFT, and Docking Studies with DNA-Targeting Potential Profiles. Int J Mol Sci. 2026;27(4):1828.
56. Bourzi H, Oukhrib R, Ibrahimi BE, Oualid HA, Abdellaoui Y, Balkard B, Hilali M, Issami SE. Understanding of Anti-Corrosive Behavior of Some Tetrazole Derivatives in Acidic Medium: Adsorption on Cu (111) Surface Using Quantum Chemical Calculations and Monte Carlo Simulations. Surf Sci. 2020;702:121692.
57. Noyel Victoria S, Prasad R, Manivannan R. Psidium guajava leaf extract as green corrosion inhibitor for mild steel in phosphoric acid. Int J Electrochem Sci. 2015;10:2220–38.
58. (a) Avci G, Corrosion inhibition of indole-3-acetic acid on mild steel in 0.5 M HCl, Colloids Surf. A. 2008;317:730–736; (b) Hany M Abd El-Lateef, Tarek El-Dabea, Mai M, Khalaf, Ahmed M, Abu-Dief. Innovation of Imine Metal Chelates as Corrosion Inhibitors at Different Media: A Collective Study, International Journal of Molecular Sciences. 2022;23:(16):9360.
59. Lebrini)M, Bentiss F, Vezin H, Lagrenée M, editors. The inhibition of mild steel corrosion in acidic solutions by 2, 5-bis (4-pyridyl)-1, 3, 4-thiadiazole: Structure–activity correlation, Corros. Sci. 2006;48(5):1279–1291; (b) Y.I. Kuznetsov, Current state of the theory of metal corrosion inhibition, Prot. Met. 2002;38:103–111.
60. Elrouby HM, El-Shafy Shilkamy MA, El-Sayed H A, Inhibitive Action of Sulfide Ions on Corrosion and Enhancing Charge-Discharge Efficiency of Zinc and Zinc- Indium Alloy as Anode for Alkaline Batteries. ChemElectroChem (, Mohamad M, Mohamed R, Shehata, Ahmed M, Abu-Dief. Targeted synthesis of two iron (III) tetradentate dibasic chelating Schiff base complexes towards inhibition of acidic induced steel corrosion: Empirical and DFT insights, Applied Organometallic Chemistry. 2022;36(7):e6718.
61. El-Lateef HM, El-Sayed AR, Mohran HS, Shilkamy HA. Corrosion inhibition and adsorption behavior of phytic acid on Pb and Pb–In alloy surfaces in acidic chloride solution. Int. J. Ind. Chem. (2019);10(1):31–47.
62. Hany M, Abd El-Lateef M, Elrouby. Hoda Abdel Shafy Shilkamy, Influence of Phytic Acid on Corrosion Behavior and Charge-Discharge Processes of Pb-2%In Alloy Anode for Lead-Acid Battery Applications. J Mol Struct. 2024;1306:137938.
63. (a)Rahman A, El-Sayed HS, Mohran HM, Abd El-Lateef H, Abdel Shafy, Shilkamy, editors. Effect of indium alloying with lead together with the addition of phosphoric acid in electrolyte to improve lead-acid battery performance, J Solid State Electrochem 2015;19:1463–1478; (b) El-Sayed A, Abd El-Shafy Shilkamy H, Elrouby M., Tracing the influence of small addition of antimony to zinc on the hydrogen evolution and anodic dissolution processes of zinc as anodes for alkaline batteries application. Int J Hydrogen Energy 2021;46(61):31239–52.
64. (a) Popova A, Sokolova E, Raicheva S, Christov M, AC and DC study of the temperature effect on mild steel corrosion in acid media in the presence of benzimidazole derivatives, Corros. Sci. (2003);45(1):33–58; (b) D.-q. Zhang, L.-x. Gao, G.-d. Zhou, Lee KY. Undecyl substitution in imidazole and its action

on corrosion inhibition of copper in aerated acidic chloride media, J. Appl. Electrochem. 2008;38:71–76.
65. (a) Bentiss F, Traisnel M, Lagrenee M, The substituted 1, 3, 4-oxadiazoles: a new class of corrosion inhibitors of mild steel in acidic media, Corrosion Science. 2000;42:127–146; (b) Achouri ME, Infante MR, Izquierdo F, Kertit S, Gouttaya HM, Nciri B. Synthesis of some cationic gemini surfactants and their inhibitive effect on iron corrosion in hydrochloric acid medium, Corrosion Science. 2001:43:19–35.
66. Verma C, Lgaz H, Verma DK, Ebenso EE, Bahadur I, Quraishi MA. Molecular dynamics and Monte Carlo simulations as powerful tools for study of interfacial adsorption behavior of corrosion inhibitors in aqueous phase: a review. J Mol Liq. 2018;260:99–120.
67. Finšgar M, Jackson J. Application of corrosion inhibitors for steels in acidic media for the oil and gas industry: A review. J Corros Sci. 2014;86:17–41.
68. (a)Li YH, Chang S, Liu XL, Huang JC, Yin JL, Wangand GL, Cao DX, editors. 2012 Nanostructured CuO directly grown on copper foam and their supercapacitance performance Electrochim. Acta. 2012;85(393):27; (b) Verma M, Kumar V and Katoch A 2017 Sputtering based synthesis of CuO nanoparticles and their structural, thermal and optical studies Mater. Sci. Semicond. Process. 2017;76:55–60.
69. (a)] L, Yu Y, Jin L, Li J, Ma G, Wang B, Geng X, Zhang, 3D porous gear-like copper oxide and their high electrochemical performance as supercapacitors CrystEngComm 15, (, Heng B, Qing C, Sun D, Wang B, Wang H, Tang Y. Rapid synthesis of CuO nanoribbons and nanoflowers from the same reaction system, and a comparison of their supercapacitor performance RSC Adv. 2013;3(36):15719–15726.
70. Dubal DP, Gund GS, Holze R. Lokhande,enhancement in supercapacitive properties of CuOthin films due to the surfactant mediated morphological modulation. J Electroanal Chem. 2014;712:40–6.
71. Wang D, Haque S, Williams T, Karim F, Hariharalakshmanan RK, Al-Mayalee KH, Karabacak T. Cyclic voltammetry and specific capacitance studies of copper oxide nanostructures grown by hot water treatment. MRS Adv. 2022;9:979–85.
72. (a)Abu-Dief AM, Nassr LAE. Tailoring, physicochemical characterization, antibacterial and DNA binding mode studies of Cu (II) Schiff bases amino acid bioactive agents incorporating 5-bromo-2-hydroxybenzaldehyde. Iran J Chem Soc. 2015;12:943. (b) L. H. Abdel-Rahman, A. M. Abu-Dief, R. M. El-Khatib, S. M. Abdel-Fatah, Sonochemical synthesis, DNA binding, antimicrobial evaluation and in vitro anticancer activity of three new nano-sized Cu (II), Co (II) and Ni (II) chelates based on tri-dentate NOO imine ligands as precursors for metal oxides, J.Photochem. Photobiol. B, Biol. 2016, 162, 298.
73. Khan SA, Rizwan K, Shahid S, Noamaan MA, Rasheed T, Amjad H. Synthesis, DFT, computational exploration of chemical reactivity, molecular docking studies of novel formazan metal complexes and their biological applications. Appl Organomet Chem. 2020;34(3):e5444.
74. Mustafa G, Rahman MZ, Sumrra SH, Ashfaq M, Zafar W, Mustafa MAG, Rahman MZ, Sumrra SH, Ashfaq M, Zafar W, Ashfaq M. A critical review on recent trends on pharmacological applications of pyrazolone endowed derivatives. J Mol Struct. 2022;1262:133044.
75. (a)El-Halim HFA, Mohamed GG, El-Dessouky MMI, Mahmoud WH. Ligational behaviour of lomefloxacin drug towards Cr (III), Mn (II), Fe (III), Co (II), Ni (II), Cu (II), Zn (II), Th (IV) and UO2 (VI) ions: Synthesis, structural characterization and biological activity studies. Spectrochim Acta A. 2011;82:8; (b) A. M. Abu-Dief, M. A. Said, O. Elhady, H. A. Al-Abdulkarim, S. Alzahrani, A. Eskander Thomas Nady, M. A. E. A. A. El-Remaily., Innovation of Fe(III), Ni(II), and Pd(II) complexes derived from benzothiazole imidazolidin-4-ol ligand: Geometrical elucidation, theoretical calculation, and pharmaceutical studies. Appl Organomet Chem 2023, 37(8), e7162.

Publisher's Note

Springer Nature remains neutral with regard to jurisdictional claims in published maps and institutional affiliations.